

Intermittent Features of the QSO Ly α Transmitted Flux: Results from Hydrodynamic Cosmological Simulations

Long-Long Feng^{1,2}, Jesus Pando³, and Li-Zhi Fang⁴

ABSTRACT

It has been recently found that the local fluctuations of the QSO's Ly α absorption spectrum transmitted flux show spiky structures. This implies that the mass fields of the intergalactic medium (IGM) is intermittent. This feature cannot be explained by the clustering evolution of cosmic mass field in the linear regimes and is also difficult to incorporate into the hierarchical clustering scenario. We calculate the structure functions and intermittent exponent of the IGM and HI for full hydrodynamical simulation samples. The result shows the intermittent features of the Ly α transmitted flux fluctuations as well as the mass field of the IGM. We find that within the error bars of current data, all the intermittent behavior of the simulation samples are consistent with the observation. This result is different from our earlier result (Pando et al 2002), which shows that the intermittent behavior of samples generated by pseudo-hydro simulation cannot be fitted with observed data. One difference between the pseudo-hydro and full hydro simulations is in treating the dynamical relation between the IGM (or HI) and dark matter fields. The former assumes that the IGM density distribution traces the underlying dark matter point-by-point on scales larger than the Jeans length in either the linear or nonlinear regimes. However, hydrodynamic studies have found that a statistical discrepancy between the IGM field and underlying dark matter in nonlinear regime is possible. We find that the point-by-point correlation between the IGM density perturbations and dark matter become weaker on comoving scales less than $2 h^{-1}$ Mpc (in LCDM model), which is larger than the IGM Jeans length.

Subject headings: cosmology: theory - large-scale structure of the universe

¹Center for Astrophysics, University of Science and Technology of China, Hefei, Anhui 230026, P.R.China

²National Astronomical Observatories, Chinese Academy of Science, Chao-Yang District, Beijing, 100012, P.R. China

³Department of Physics, DePaul University, Chicago Il, 60614

⁴Department of Physics, University of Arizona, Tucson, AZ 85721

1. Introduction

In the past few years there has been tremendous progress in understanding the evolution of cosmic structures on scales from galaxies to about $100 h^{-1}$ Mpc. This progress has occurred mainly in two distinct areas: 1.) constraining cosmological parameters such as the mass density, dark energy, power spectrum of the initial perturbations of the cosmic mass field, etc., 2.) the modeling of the origin of light-emitting objects to explain the observed mass density profiles, velocity dispersions, mass-to-light ratios, substructures, bias behavior, etc., of quasars, galaxies and galaxy clusters.

These two distinct areas coincide with two different regimes in the context of the dynamics of structure formation. The first one is based mainly on the evolution of the cosmic mass field in the linear approximation. The basic statistical tool is the power spectrum, either observed or recovered by Gaussianization, of the weakly non-linear field. The second regime is characterized by the dynamics of collapsed massive halos. The formation and evolution of luminous clumps can be modeled by the growing and merging of massive halos from initially Gaussian perturbations of the mass and velocity fields. The hierarchical clustering of halos is the most effective scenario for modeling galaxy formation.

However, the clustering behavior of the mass and velocity fields of Inter-Galactic Medium (IGM), i.e., the major component of baryonic matter in the universe, is missing from these two regimes. It is certain that the IGM field is not linear and Gaussian because the distributions of QSO's Ly α forests from either observational data or simulation samples (Bi 1993, Bi, Ge & Fang 1995), have been found to be non-Gaussian even on scales as large as a few h^{-1} Mpc (Pando & Fang 1996, 1998a). Neither is the evolution of the IGM field well modeled by the dynamics of collapsing halos, as the QSO's Ly α forests are generally not gravitationally confined (Fang et al 1996). The success of modeling the QSO's Ly α forests via a lognormal model of the IGM (Bi & Davidsen 1997) directly indicates that the IGM field probably does not (or has not yet) undergone a correlation hierarchy evolution.

The clustering behavior of the IGM mass field can play an important role in the dynamical gap between linear power spectrum and collapsed massive halos. For instance, it has recently been found that the QSO Ly α transmitted flux fluctuations are intermittent (Jamkhedkar, Zhan & Fang 2000, Feng, Pando & Fang 2001, Zhan, Jamkhedkar & Fang 2001). A field is intermittent if the $2n^{th}$ power of the local differences grows faster than the n^{th} power of the variance of these differences (see Section 2.) This result cannot be found using the statistical tools of the linear regime such as power spectrum. At the same time, it is unclear how to incorporate intermittent behavior with the hierarchical clustering scenario. The intermittent features have also been studied with simulated Ly α forests produced by a pseudo hydro technique. All the pseudo hydro samples for low density cold dark matter (LCDM) and warm dark matter (WDM) models are found to be substantially intermittent. Although the intermittent features of the simulation samples were different from those of the observations (Pando et al 2002), the results implies that intermittency

is a common feature of non-linear evolution and is potentially useful for model discrimination.

This motivated us to re-do the intermittent analysis with simulated Ly α transmitted fluxes produced by a full hydrodynamical treatment. This motivation was strengthened when we realized that the relation between the IGM and dark matter fields in the non-linear regime is treated differently in the pseudo-hydro and full hydro simulations. In the pseudo-hydro simulation, the density of the IGM in each pixel is assigned according to the dark matter density at that pixel. That is, the pseudo-hydro simulation assumes that the density distribution of IGM traces the underlying dark matter point-by-point on scales larger than the Jeans length in either the linear or nonlinear regimes. This assumption looks reasonable when one considers that the IGM is only a passive substance in the cosmic mass field since its evolution is dominated by the gravity of dark matter.

However, hydrodynamic studies have shown that a passive substance in the system does not always behave like the underlying dominant mass field when non-linear evolution has taken place (for a review, Shraiman & Siggia 2001). The statistical properties of a passive substance can *decouple* from those of the underlying field. As we show here, the dynamical equations of the IGM within the gravitational field of dark matter are the same as that used for describing the statistical decoupling between the passive substance and underlying field. Therefore, it is possible there is a statistical discrepancy between the IGM field and underlying dark matter in nonlinear regime.

The purpose of this paper is then two-fold. First we study whether the intermittency of the QSO Ly α transmitted flux is matched by the full hydro simulation samples. Secondly we search for possible signs of the statistical discrepancy between the IGM field and the underlying dark matter with these samples. The paper is organized as follows. §2 presents a brief introduction to intermittent fields and the method to quantify intermittent random fields. §3 describes the observed samples that we use. §4 describes full hydrodynamic simulations. The statistical deviation of the IGM distribution from the dark matter field is shown in §5. A comparison between the model predicted and observed intermittency is performed in §6. Finally, the conclusions and discussions are presented in §7. The dynamical equations for the IGM evolution in non-linear regime is given in Appendix.

2. Intermittency

Much of this section has been presented in our previous work (Pando et al 2002). For the paper to be self-contained, we repeat these results briefly.

2.1. The intermittent exponent

Intermittency is used to characterize a random field with ‘spike-gap-spike’ features, i.e., structures that are essentially strong enhancements randomly and widely scattered in space and/or time, with a low field value between the spikes. The spike-gap-spike feature is more pronounced on smaller scales. This feature was originally found in the temperature and velocity distributions in turbulence (Batchelor & Townsend 1949; Frisch 1995).

An intermittent random density field $\rho(\mathbf{x})$ is defined by the asymptotic behavior (indicated below by \asymp) of the ratio between the high- and low-order moments of the field as (Gärtner & Molchanov, 1990; Zel’dovich, Ruzmaikin, & Sokoloff, 1990)

$$\frac{\langle [\rho(\mathbf{x} + \mathbf{r}) - \rho(\mathbf{x})]^{2n} \rangle}{[\langle [\rho(\mathbf{x} + \mathbf{r}) - \rho(\mathbf{x})]^2 \rangle]^n} \asymp \left\langle \frac{r}{L} \right\rangle^\zeta, \quad (1)$$

where L is the size of the sample. Intermittency is measured by the n - and r -dependencies of ζ – the intermittent exponent. If the exponent ζ is negative on small scales r , the field is intermittent. That is, the ratio in eq. (1) for an intermittent field diverges as $r \rightarrow 0$.

This divergence cannot be measured by individual higher order correlation functions. Although three- and four-point correlation functions are useful for distinguishing a Gaussian from a non-Gaussian field, they are insensitive to the difference between an intermittent field and a non-Gaussian, but non-intermittent field. To measure intermittency, we define the structure function as

$$S_r^{2n} = \langle |\Delta_r(x)|^{2n} \rangle \quad (2)$$

where $\Delta_r(x) \equiv \rho(x+r) - \rho(x)$, and $\langle \dots \rangle$ is the average over the ensemble of fields. If the field is statistically homogeneous, S_r^{2n} is independent of x and depends only on r . S_r^{2n} is called the structure function. When $n = 1$, we have

$$S_r^2 = \langle |\Delta_r(x)|^2 \rangle. \quad (3)$$

S_r^2 is the mean of the square of the density fluctuations at wavenumber $k \simeq 2\pi/r$, and therefore, S_r^2 is the power spectrum of the field. With the structure function, eq.(1) can be rewritten as

$$\frac{S_r^{2n}}{[S_r^2]^n} \propto \left(\frac{r}{L} \right)^\zeta. \quad (4)$$

The ratio $S_r^{2n}/(S_r^2)^n$ is the n^{th} moment S^{2n} normalized by the power S^2 . Since S_r^2 measures the width of the probability distribution function (PDF) of $|\Delta_r(x)|$, while S_r^{2n} is sensitive to the tail of the PDF, the ratio eq.(4) measures the fraction of density fluctuations in the tail on different scales.

For an intermittent field the ratio of S_r^{2n} to $[S_r^2]^n$ is larger for smaller r and indicates that the field contains “abnormal” events of large density fluctuations $|\Delta_r(x)|$. That is, the PDF of $|\Delta_r(x)|$ is long-tailed. The long-tail events correspond to a sharp increase or decrease of the density $\rho(\mathbf{x})$.

They are rare events and yield high peaks or spikes in the distribution of density difference. Generally speaking, the intermittent exponent ζ measures the smoothness of the field: for positive ζ , the field is smoother on smaller scales. If ζ is negative, the field is rough on small scales.

The basic quantity used for calculating the intermittent exponent ζ is the density difference $|\Delta_r(x)|$. The exponent ζ does not rely on the mean density $\bar{\rho}$ and can be measured even if the mass field is fractal, in which case the mean density is no longer available.

2.2. Examples of the intermittent exponent

In our previous work we presented several examples of intermittency in various kinds of fields. Here we summarize those results for the kinds of fields that pertain to this work.

For a Gaussian field,

$$\frac{S_r^{2n}}{[S_r^2]^n} = (2n - 1)!! \quad (5)$$

This ratio is independent of scale r , and therefore, the intermittent exponent $\zeta = 0$. A Gaussian field is not intermittent. A self-similar field is also not intermittent.

For a hierarchically clustered field, it has been shown (Feng, Pando, & Fang 2001) that

$$\frac{S_r^{2n}}{[S_r^2]^n} \propto \left(\frac{r}{L}\right)^{-(d-\kappa)(n-1)}, \quad (6)$$

where d is the spatial dimension, and the coefficient κ is a constant depending on the power law index of the power spectrum. In the case where $\kappa < d$, the field is intermittent with exponent

$$\zeta \simeq -(d - \kappa)(n - 1). \quad (7)$$

Finally, for a lognormal field the PDF of $\Delta_r(x)$ is given by

$$P[\Delta_r(x)] = \frac{1}{2^{3/2}\pi^{1/2}|\Delta_r(x)|\sigma(r)} \exp\left\{-\frac{1}{2}\left(\frac{\ln|\Delta_r(x)| - \ln|\Delta_r(x)|_m}{\sigma(r)}\right)^2\right\}, \quad (8)$$

where $|\Delta_r(x)|_m$ is the *median* of $|\Delta_r(x)|$ (Vanmarcke 1983). The variance $\sigma(r)$ of $\ln|\Delta_r(x)|$ generally can be a function of the scale r . Using eq.(8), we have

$$\frac{S_r^{2n}}{[S_r^2]^n} = e^{2(n^2-n)\sigma^2(r)}. \quad (9)$$

The intermittent exponent of a lognormal field is then

$$\zeta \simeq 2(n^2 - n)\sigma^2(r)/\ln(r/L). \quad (10)$$

Because $r < L$, ζ is negative. Therefore, a lognormal field is intermittent.

To summarize, the structure function and intermittent exponent provide a complete and unified description of intermittent fields. The n - and r -dependencies of the structure functions and intermittent exponent ζ are sensitive to the details of the intermittency of the field. These measures are very powerful for distinguishing among fields that are Gaussian, self-similar, mono-fractal, multi-fractal, and singular.

2.3. The intermittent exponent in the wavelet basis

The quantity $\Delta_r(x)$ or $[\rho(x+r) - \rho(x)]$ contains two variables: the position x and the scale r , and therefore, $\rho(x+r) - \rho(x)$, can best be calculated with a space-scale decomposition. Among the mathematical tools used to decompose functions in scale space as well as physical space, the discrete wavelet transform (DWT) is an excellent choice. The DWT basis are orthogonal and complete, and therefore, the DWT decomposition does not lose information (completeness), and does not cause false correlations due to redundancy (non-orthogonality). These two points are essential in studying the higher order statistical features of random fields.

We restrict our discussion to a 1-D random field $\rho(x)$ extending in a physical or redshift spaces $L = x_2 - x_1$. To apply the DWT, we first chop the spatial range $L = x_2 - x_1$ into 2^j subintervals labeled $l = 0, \dots, 2^j - 1$ where j is a positive integer. Each subinterval spans a spatial range $L/2^j$ with the l^{th} subinterval spanning from $x_1 + Ll/2^j$ to $x_1 + L(l+1)/2^j$. This operation decomposes the space L into cells (j, l) , where j denotes the scale $L/2^j$, and l the spatial range.

Corresponding to each cell, there is a scaling function $\phi_{jl}(x)$, and a wavelet function $\psi_{jl}(x)$. The scaling function $\phi_{j,l}(x)$ is a window function on scale j and at position l . The wavelet functions $\psi_{jl}(x)$ form the basis for the scale-space decomposition. The most important property of the DWT basis is its locality in both scale and physical spaces.

With the DWT, a density field $\rho(x)$ can be decomposed as (Fang & Thews 1998).

$$\rho(x) = \sum_{l=0}^{2^j-1} \epsilon_{j,l} \phi_{jl}(x) + \sum_{j'=j}^J \sum_{l=0}^{2^{j'}-1} \tilde{\epsilon}_{j',l} \psi_{j',l}(x), \quad (11)$$

where J is given by the finest scale (resolution) of the sample, i.e., $\Delta x = L/2^J$, and j is the scale of interest. The scaling function coefficient (SFC) ϵ_{jl} in eq.(11) is given by projecting $\rho(x)$ onto $\phi_{j,l}(x)$

$$\epsilon_{j,l} = \int \rho(x) \phi_{j,l}(x) dx. \quad (12)$$

The SFC ϵ_{jl} describes the mean field of the mode (j, l) .

The wavelet function coefficient (WFC), $\tilde{\epsilon}_{j,l}$, in eq.(11) is obtained by projecting $\rho(x)$ onto $\psi_{j,l}(x)$

$$\tilde{\epsilon}_{j,l} = \int \rho(x) \psi_{j,l}(x) dx. \quad (13)$$

The wavelet function $\psi_{jl}(x)$ is admissible (Daubechies 1992), i.e., $\int \psi_{jl}(x)dx = 0$, so the WFC is basically the difference between $\rho(x)$ and $\rho(x+r)$, where $x \simeq x_1 + lL/2^j$ and $r \simeq L/2^j$. Therefore, the WFC eq.(13) measures the fluctuation on scale j and at position l . Because the admissibility of wavelets, eq.(13) can also be written as

$$\tilde{\epsilon}_{j,l} = \int \delta(x)\psi_{j,l}(x)dx, \quad (14)$$

if the normalization is $\bar{\rho} = 1$. Thus, the WFC can be used as the variable $\rho(x+r) - \rho(x)$ or $\delta(x+r) - \delta(x)$ in eq.(2). All compactly supported wavelet bases produce similar results. We will use Daubechies 4 (Daubechies, 1992) in the study below.

When the “fair sample hypothesis” is applicable (Peebles 1980), the structure function eq.(2) can be calculated as the spatial average

$$S_r^{2n} = \frac{1}{L} \int |\Delta_r(x)|^{2n} dx, \quad (15)$$

where L is the spatial range of the sample. In the DWT representation, eq.(15) yields

$$S_j^{2n} = \langle |\tilde{\epsilon}_{j,l}|^{2n} \rangle = \frac{1}{2^j} \sum_{l=0}^{2^j-1} |\tilde{\epsilon}_{j,l}|^{2n}, \quad (16)$$

where j plays the same role as r in eq.(2). S_j^{2n} is the mean of moment $|\tilde{\epsilon}_{j,l}|^{2n}$ over the position index l . The intermittent exponent ζ in eq.(4) can be calculated from

$$\frac{S_j^{2n}}{[S_j^2]^n} \propto 2^{-j\zeta}. \quad (17)$$

Generally, ζ depends on n and j .

3. The Observed Ly α transmitted flux

3.1. QSO’s Ly α absorption spectra

The observed transmitted flux at wavelength λ is $F(\lambda) = F_c e^{-\tau(\lambda)}$, where $\tau(\lambda)$ is optical depth, and F_c the continuum which is generally λ -dependent. F_c is given by the emission spectrum of the QSO considered. To study the intermittent behavior of the IGM we focus on the fluctuation field $e^{-\tau(\lambda)}$. The intermittent features of transmitted flux of QSO’s Ly α absorption spectrum were previously studied with a set of about 30 Keck HIRES spectra (Jamkhedkar, Zhan, & Fang, 2000, Pando et al. 2002). This work will consider the two best absorption spectra in that the sample set.

1. HS1700+6416

The absorption spectrum of QSO HS1700+6416 (redshift $z = 2.72$) covers a wavelength range from 3727.012 Å to 5523.554 Å, for a total of 55882 pixels. On average, a pixel is about 0.028 Å. For

all pixels in this data set, the ratio $\Delta\lambda/\lambda \simeq 7 \times 10^{-6}$ and constant, or in terms of the local velocity, $\delta v = c\Delta\lambda/\lambda \simeq 2.1$ km/s, and therefore, the resolution is about 4 km/s. The distance between N pixels in units of the local velocity scale is given by $\Delta v = 2c(1 - \exp[-(1/2)N \delta v/c])$ km/s, or wavenumber $k = 2\pi/\Delta v$ s/km. As $\delta v/c \ll 1$, we have $\Delta v \simeq N \delta v$. In this work, we use the data from $\lambda = 3815.6 \text{ \AA}$ to 4434.3 \AA , which corresponds to $z = 2.14 \sim 2.65$. The lower limit of the wavelength is set to exclude Ly β absorption, the upper to eliminate proximity effects. The continuum F_c for this spectrum was done by IRAF CONTINUUM fitting by Kirkman and Tytler (1997).

In each pixel the data contain wavelength λ_i , flux $F(\lambda_i)$ and noise $\sigma(\lambda_i)$, which accounts for the Poisson fluctuations in the photon count, the noise due to the background and the instrumentation. The S/N ratio is about 8.

This data set contains a fitted flux which smooths out all fluctuations on smallest scales, i.e. one or two pixels. The fluctuations on these scales are substantially suppressed by the fitting procedure. However, we analyze only scales greater than or equal to 16 pixels. Therefore, the smoothing has little effect on our results. Metal lines for this spectrum have been identified down to the Doppler parameters $b \sim 10$ km/s by Wei Zheng (unpublished).

2. *q0014+8118*

This spectra has the highest S/N ~ 30 among the 30 Keck QSO spectra collected by Kirkman and Tytler (1997). The redshift of q0014+8118 is 3.387. For all pixels in this data set $\Delta\lambda/\lambda \simeq 13.8 \times 10^{-6}$, or $\delta v = c\Delta\lambda/\lambda \simeq 4.01$ km/s, and, therefore, the resolution is about 8 km/s. In each pixel, the data also contains wavelength λ_i , flux $F(\lambda_i)$ and noise $\sigma(\lambda_i)$. The continuum of the spectrum is given by IRAF CONTINUUM fitting as well.

We use the wavelength region from the Ly β emission to the Ly α emission, excluding a region of about 0.06 in redshift close to the quasar to avoid any proximity effects. This corresponds to $z = 2.702$ to 3.314 , which contains 12703 pixels. The distance between N pixels in the units of the local velocity scale is given by $\Delta v \simeq N \times 4.01$ km/s, or wavenumber $k = 2\pi/\Delta v$ s/km. Absorption features with $b < 20$ km s $^{-1}$ of this spectrum have been identified.

3.2. Treatment of unwanted data

To study the intermittency of the transmission flux fluctuations, we should remove the effects of unwanted data, such as 1.) bad pixels (gaps without data), 2.) metal lines, and 3.) negative flux pixels. The last category generally consists of saturated absorption regions having lower S/N . Although the percentage of low S/N data is not large, it will introduce large uncertainties in the analysis.

The conventional technique for removing unwanted data is to eliminate the unwanted bins and to smoothly rejoin the rest of the forest spectra. However, by taking advantage of the localization

of wavelets we can use the algorithm of DWT de-noising by thresholding (Donoho 1995) as follows

1. Calculate the SFCs for both the transmission $F(\lambda)$ and noise $\sigma(\lambda)$, i.e.

$$\epsilon_{jl}^F = \int F(x)\phi_{jl}(x)dx, \quad \epsilon_{jl}^N = \int \sigma(x)\phi_{jl}(x)dx. \quad (18)$$

2. Identify unwanted mode (j, l) using the condition

$$\left| \frac{\epsilon_{jl}^F}{\epsilon_{jl}^N} \right| < f \quad (19)$$

where f is a constant. This condition flags all modes with S/N less than f . We can also flag modes dominated by metal lines.

3. Since all the statistical quantities in the DWT representation are based on an average over the modes (j, l) , we do not count all the flagged modes when computing these averages.

This is the conditional-counting method to treat the unwanted data (Pando et al. 2002).

It should be emphasized that the condition (19) is applied at each scale j . For instance, if the size of a saturated absorption region is d , eq.(19) requires the removal of all modes (j, l) on scales less than d and located within this region, as these modes have very low S/N ($\epsilon_{jl}^F/\epsilon_{jl}^N < f$) and the local fluctuations in these regions are not reliable. However, condition (19) does not require the removal of the saturated absorption region when d is less than the scale of modes (j, l) considered. If $\epsilon_{jl}^F/\epsilon_{jl}^N > f$, the mode (j, l) is counted in the statistics, regardless of whether the mode (j, l) contains the saturated absorption regions. The DWT analysis allows an effective application of data containing low S/N regions. That is, with the scale-by-scale denoising, it eliminates low S/N modes on small scales and in these regions, but keeps their contributions to large scale modes. With this procedure, no eliminating and smoothly rejoining of the data is needed, and therefore, it avoids corrupting long wavelength modes.

With this method, we can still calculate the structure functions by eq.(17), but the average is not over all modes l , but over the un-flagged modes only. We can also flag modes (j, l) one by one which are dominated by metal lines. Since the DWT calculation assumes the sample is periodized, this may cause uncertainty at the boundary. To reduce this effect, we drop 3 modes near the boundary, and also flag two modes around a unwanted mode to reduce any boundary effects of the chunks.

3.3. Power spectrum of HS1700

To check the quality of the data, we calculate the power spectrum of the transmitted flux fluctuations, $\Delta F = F(\lambda) - \langle F(\lambda) \rangle$, of HS1700+6416. In the DWT representation, this power

spectrum is given by (Pando & Fang 1998b; Fang & Feng 2000, Jamkhedkar, Bi, & Fang, 2001)

$$P_j = \frac{1}{2^j} \sum_{l=0}^{2^j-1} (\tilde{\epsilon}_{jl}^F)^2 - \frac{1}{2^j} \sum_{l=0}^{2^j-1} (\tilde{\epsilon}_{jl}^n)^2. \quad (20)$$

The first term on the r.h.s. of eq.(20) is the power of ΔF on scale j , in which the wavelet coefficients (WFC) $\tilde{\epsilon}_{jl}^F$ are given by

$$\tilde{\epsilon}_{jl}^F = \int F(x) \psi_{jl}(x) dx. \quad (21)$$

The second term on the r.h.s. of eq.(20) is due to the noise field $\sigma(\lambda)$ and calculated by

$$(\tilde{\epsilon}_{jl}^n)^2 = \int \sigma^2(x) \psi_{jl}^2(x) dx. \quad (22)$$

The DWT power spectrum P_j of a random field $F(x)$ is related to its Fourier power spectrum $P(n)$ by

$$P_j = \frac{1}{2^j} \sum_{n=-\infty}^{\infty} |\hat{\psi}(n/2^j)|^2 P(n). \quad (23)$$

where $\hat{\psi}$ is the Fourier transform of the wavelet. This implies that the DWT power spectrum P_j is the banded Fourier power of the flux fluctuations $F(\lambda) - \langle F(\lambda) \rangle$. Since for D4 wavelet $|\hat{\psi}(\eta)|^2$ is peaked at $\eta \simeq 1$, the band j corresponds to the wavenumber $k = 2\pi n/L \simeq 2\pi 2^j/L$.

Figure 1 plots the results of the power spectra for HS1700+6416, in which the data is treated three ways, 1.) using the original fitted flux, 2.) using the conditional counting method eq.(19) with $f = 1$, and 3.) with $f = 3$.

At the first glance, the conditional-counting condition eq.(19) would seem to preferentially miss-count modes in the low transmission regions and lead to an f -dependence in the power spectrum. However Fig. 1 shows that the power spectrum P_j is independent of f on entire the scale range considered from $f = 1$ to 3. The reason can be seen from eq.(20), which shows that the contribution to the power P_j given by mode (j, l) is $(\tilde{\epsilon}_{jl}^F)^2 - (\tilde{\epsilon}_{jl}^n)^2$. The noise subtraction term $(\tilde{\epsilon}_{jl}^n)^2$ guarantees that the contribution of modes with small ratio S/N to P_j is always small or negligible. In other words, all the miss-counted modes make very small or negligible contributions to P_j regardless the parameter f .

Also in Fig. 1, on scales $j > 10$, or $\Delta v < 32$ km/s, the power of the fitted flux is lower than the power spectrum. This discrepancy is probably because the fitted flux is over-suppressed, i.e., not only noise, but also real fluctuations are suppressed by the fitting procedure. This discrepancy indicates that the effects of noise become significant on scales $\Delta v < 32$ km/s. For this reason, we use only data on scales $\Delta v \geq 32$ km/s. Sample q0014+8118 is of similar quality and for it we also only use scales $\Delta v \geq 32$ km/s.

4. Hydrodynamical simulations

4.1. The simulation

For the hydrodynamic simulations, we use a Eulerian code based on a weighted essentially non-oscillatory (WENO) scheme for a hyperbolic system (Jiang & Shu, 1996; Shu, 1998). WENO realizes the idea of adaptive stencils in the reconstruction procedure based on the local smoothness of the numerical solution to automatically achieve high order accuracy and non-oscillatory property near discontinuities. It is extremely robust and stable for solutions containing strong shock and complex solution structures. This is especially important in studying intermittency. In the context of cosmological applications, we developed a hybrid N-body/hydrodynamical code that incorporates a Lagrangian particle-mesh algorithm to evolve the collision-less matter with the fifth order WENO scheme to solve the equation of gas dynamics (Feng et.al, 2002).

In the present application, we computed the cosmic evolution of the coupled system of both dark matter and baryonic matter in a flat low density CDM model (Λ CDM), which is specified by the density parameter $\Omega_m = 0.3$, cosmological constant $\Omega_\Lambda = 0.7$, Hubble constant $h = 0.7$, and mass fluctuation within a sphere of radius $8h^{-1}\text{Mpc}$, $\sigma_8 = 0.9$. The baryon fraction is fixed using the constraint from primordial nucleosynthesis as $\Omega_b = 0.0125h^{-2}$ (Walker et.al, 1991). The linear power spectrum is taken from the fitting formulae presented by Eisenstein & Hu (1998). We perform the simulations in a 128^3 grid with an equal number of dark matter particles. In order to examine the effects of numerical resolution, two simulations on a periodic, cubical box of size $6h^{-1}\text{Mpc}$ and $12h^{-1}\text{Mpc}$ are generated. The simulations start at a redshift $z = 49$ and the results were outputed at the average redshifts of the each observation samples (for q0014+8118, $z_m = 2.915$, and HS1700+6416, $z_m = 2.329$). The timestep is chosen by the minimum value among three time scales. The first is from the Courant condition given by

$$\delta t \leq \frac{cfl \times a(t)\Delta x}{\max(|u_x| + c_s, |u_y| + c_s, |u_z| + c_s)} \quad (24)$$

where Δx is the cell size, c_s is the local sound speed, u_x , u_y and u_z are the local fluid velocities and cfl is the Courant number, typically, we take $cfl = 0.6$. The second constraint is imposed by cosmic expansion which requires that $\Delta a/a < 0.02$ within single time step. The last constraint comes from the requirement that a particle move no more than a fixed fraction of cell size in one time step.

Atomic processes including ionization, radiative cooling and heating are modeled as in Cen (1996) in a primeval plasma of hydrogen and helium of composition ($X = 0.76$, $Y = 0.24$). The uniform UV-background of ionizing photons is assumed to have a power-law spectrum of the form $J(\nu) = J_{21} \times 10^{-21}(\nu/\nu_{HI})^{-\alpha}\text{ergs}^{-1}\text{cm}^{-2}\text{sr}^{-1}\text{Hz}^{-1}$, where the photoionizing flux is normalized by parameter J_{21} at the Lyman limit frequency ν_{HI} , and is suddenly switched on at $z \sim 6$ to heat the gas and reionize the universe.

One-dimensional fields are extracted along randomly selecting lines of sight in the simulation

box. The density, temperature and velocity of the neutral gas fraction on grids are firstly Gaussian smoothed using FFT techniques which form the fundamental data set. The one-dimensional grid containing the physical quantities is further interpolated by a cubic spline. Using this one-dimensional grid, the optical depth τ at each pixel is then obtained by integrating in real space and we include the effect of the peculiar velocity and convolve with Voigt thermal broadening. To have a fair comparison with observed spectra, τ was Gaussian smoothed to match with the spectral resolutions of observation. The transmitted flux $F = \exp(-\tau)$ is normalized such that the mean flux decrement in the spectra match with observations.

Each mock spectrum is sampled on a 2^{10} grid with the same spectral resolution as the observation. As the corresponding comoving scale for 2^{10} pixels is larger than the simulation box size, we replicate periodically the sample. To achieve the greatest the statistical independence, we randomly change the direction of line of sight while crossing the boundary of the simulation box. For each observed spectrum, 1000 mock spectra are generated. In addition, we also output 100 samples of the density distribution of both dark matter and neutral hydrogen on the one-dimensional grid.

4.2. Power spectrum of hydrodynamical simulation samples

Figure 2 compares the DWT power spectra measured in the mock samples and the observed data of HS1700. The comoving wavelength k in Fig. 2 is given by $k = 2\pi/L$, where $L = (\Delta v/H_0)[\Omega_m(1+z_m)^3 + \Omega_\Lambda]^{-1/2}$. The $1-\sigma$ errors for the simulation samples are derived from the 1000 mock spectra. For the observed spectrum of HS1700, we divide the first 2^{14} pixels of the observed spectrum into 16 subsections, each with 2^{10} pixels. The DWT power spectra are obtained for each subsection respectively, and the $1-\sigma$ error is estimated from the variance of the 16 sections. [For an intermittent field, the error estimation of power spectrum is sensitively dependent on how one treats the intermittency (Jamkhedkar, 2002). We do not discuss the details of this point here as it will not affect the following discussion.]

Figure 2 shows that simulation samples with the 12 Mpc box are in good agreement with observations on all scales $k \leq 15 \text{ h Mpc}^{-1}$, which corresponds to $j = 10$ in Fig. 1. The simulation samples with the $6 \text{ h}^{-1}\text{Mpc}$ box have higher power than observed sample on small scales, but lower power on large scales. This is expected because the simulation in the $6 \text{ h}^{-1}\text{Mpc}$ box lacks perturbations on scales $k \leq 1 \text{ h Mpc}^{-1}$ and the normalization of the mean flux decrement will lead to the higher power on small scales to compensate for the loss of powers on large scales.

On small scales $k > 15 \text{ h Mpc}^{-1}$, the simulated power is significantly lower than the observation data. This shows again that noise contamination becomes important on scales $k > 15 \text{ h Mpc}^{-1}$, or $j > 10$. Therefore, as in §3.3, we use the simulation data only on scales $k > 15 \text{ h Mpc}^{-1}$, or $j \leq 10$, or $\Delta v \geq 32 \text{ km/s}$.

5. Statistical discrepancy between baryonic gas and dark matter

5.1. Relation between IGM and dark matter mass fields

It is well known that in the linear approximation the density contrast of the IGM, $\delta_b(\mathbf{x}, t)$ is equal to that of dark matter $\delta_{DM}(\mathbf{x}, t)$ on scales larger than the Jeans length. This is true even if initially $\delta_b(\mathbf{x}, t_0) \neq \delta_{DM}(\mathbf{x}, t_0)$ (Bi, Börner & Chu 1993, Nusser 2000, Matarrese & Mohayee 2002). In other words, the density fluctuations of the IGM trace the dark matter fields point-by-point. Since the clustering of the IGM is governed by the gravity of dark matter, the IGM can be considered as "passive substance" with respect to the underlying dark matter. Thus, the point-by-point relations $\rho_b(\mathbf{x}, t) \propto \rho_{DM}(\mathbf{x}, t)$ and $\delta_b(\mathbf{x}, t) = \delta_{DM}(\mathbf{x}, t)$ on scales larger than the Jeans length also looks reasonable in the nonlinear regime. In this case, *all* the statistical properties of the IGM field on scales larger than the Jeans length are the same as the underlying dark matter field.

However, it is known that a passive substance in a hydrodynamic system does not always behave like the underlying dominant mass field when non-linear evolution takes place. The statistical properties of a passive substance can *decouple* from those of the underlying field in the nonlinear regime. Moreover, the evolution of the IGM driven by the gravitational field of dark matter is described by a non-linear equation which is essentially the same as that used for modeling the statistical decoupling between a passive substance and its underlying field (see Appendix A.) Hence, we expect to see a statistical discrepancy between $\delta_b(\mathbf{x}, t)$ and $\delta_{DM}(\mathbf{x}, t)$ on scales larger than the Jeans length.

To determine whether any statistical decoupling has occurred, we begin by assuming that $\delta_b(\mathbf{x}, t) = \delta_{DM}(\mathbf{x}, t)$. Then wavelet transforming yields $\tilde{c}_{jl}^b = \tilde{c}_{jl}^{DM}$, and therefore

$$\langle \tilde{c}_{jl}^b \tilde{c}_{jl}^{DM} \rangle = \langle [\tilde{c}_{jl}^b]^2 \rangle = \langle [\tilde{c}_{jl}^{DM}]^2 \rangle. \quad (25)$$

$\langle [\tilde{c}_{jl}^b]^2 \rangle$ and $\langle [\tilde{c}_{jl}^{DM}]^2 \rangle$ are, respectively, the DWT power spectrum of the IGM and dark matter fields. Therefore, the first conclusion of the point-by-point relation $\delta_b(\mathbf{x}, t) = \delta_{DM}(\mathbf{x}, t)$ is that the power spectra of the IGM and dark matter should be the same. Figure 3 indeed shows that the power spectra of the IGM and dark matter fields are about the same.

With eq.(24), it is obvious that the power spectrum of the field $\delta_b(\mathbf{x}, t) - \delta_{DM}(\mathbf{x}, t)$ should be equal to zero, or considering noise, very small. Figure 4 gives the power spectra $\langle [\tilde{c}_{jl}^b - \tilde{c}_{jl}^{DM}]^2 \rangle$ and $\langle [\tilde{c}_{jl}^b]^2 \rangle$ and shows that on large scales $j < 8$ ($\Delta v > 128$ km/s) $\langle [\tilde{c}_{jl}^b - \tilde{c}_{jl}^{DM}]^2 \rangle$ is much less than $\langle [\tilde{c}_{jl}^b]^2 \rangle$. The ratio of $\langle [\tilde{c}_{jl}^b - \tilde{c}_{jl}^{DM}]^2 \rangle$ to $\langle [\tilde{c}_{jl}^b]^2 \rangle$ is < 0.05 , which probably is due to noise. However, on scales $j \geq 8$ ($\Delta v \geq 128$ km/s), this ratio gradually increases to $\simeq 0.4$. This difference between large and small scales cannot be explained by the noise, as can be seen from Fig. 2 in which the error bars in the range $1 < k < 10$ h⁻¹ Mpc (corresponding to $j = 7$ to 10) are about the same. Figure 4 indicates that $\langle \tilde{c}_{jl}^b \tilde{c}_{jl}^{DM} \rangle < \langle [\tilde{c}_{jl}^b]^2 \rangle$ on small scales, i.e., the point-by-point correlation between the IGM density fields and dark matter fields is weaker on small scales. This is a sign of the statistical discrepancy between the IGM and dark matter mass fields.

We can further make the case by calculating the structure functions for the field $\delta_b(\mathbf{x}, t) - \delta_{DM}(\mathbf{x}, t)$. The result is plotted in Fig. 5 and shows that for $j = 6$ the ratio of the moments is Gaussian, i.e. $\ln S_j^{2n}/(S_j^2)^n = \ln(2n - 1)!!$ [eq.(5)]. On scales $j \geq 8$, $\ln S_j^{2n}/(S_j^2)^n$ is significantly larger than a Gaussian distributions which strongly indicates of the statistical discrepancy between $\delta_b(\mathbf{x}, t)$ and $\delta_{DM}(\mathbf{x}, t)$ is not due to noise. For a given n , $\ln S_j^{2n}/(S_j^2)^n$ increases with scale j so that the intermittent exponent ζ [eq.(21)] is non-zero and negative, and therefore, the field $\delta_b(\mathbf{x}, t) - \delta_{DM}(\mathbf{x}, t)$ is intermittent. This result is consistent with the dynamical equation (A14), which requires that the difference $\delta_b(\mathbf{x}, t) - \delta_{DM}(\mathbf{x}, t)$ generally is an intermittent field. Thus, we conclude again that there is statistical discrepancy from the point-by-point relation $\delta_b(\mathbf{x}, t) = \delta_{DM}(\mathbf{x}, t)$.

5.2. Relation between HI and dark matter

The statistical discrepancy in the relation between the density fields of neutral hydrogen and dark matter is important as well. For instance, the pseudo-hydro technique assumes that $\delta_{HI}(\mathbf{x}, t) \propto \delta_{DM}^a(\mathbf{x}, t)$ with $1.5 < a < 1.9$ (Hui & Gnedin, 1997). This relation yields $\langle \tilde{\epsilon}_{jl}^{HI} \tilde{\epsilon}_{jl}^{DM} \rangle > 0$, and therefore the power spectrum $\langle [\tilde{\epsilon}_{jl}^{HI} + \tilde{\epsilon}_{jl}^{DM}]^2 \rangle$ should be larger than $\langle [\tilde{\epsilon}_{jl}^{HI} - \tilde{\epsilon}_{jl}^{DM}]^2 \rangle$. Figure 6 presents the power spectra $\langle [\tilde{\epsilon}_{jl}^{HI} \pm \tilde{\epsilon}_{jl}^{DM}]^2 \rangle$ and shows $\langle [\tilde{\epsilon}_{jl}^{HI} + \tilde{\epsilon}_{jl}^{DM}]^2 \rangle > \langle [\tilde{\epsilon}_{jl}^{HI} - \tilde{\epsilon}_{jl}^{DM}]^2 \rangle$ on large scales, but this difference is significantly smaller on smaller scales.

Figure 7 gives the power spectra $\langle [\tilde{\epsilon}_{jl}^{HI} - \tilde{\epsilon}_{jl}^{DM}]^2 \rangle$ and $\langle [\tilde{\epsilon}_{jl}^b]^2 \rangle$ and reveals that it is similar to Fig. 4. All the results indicate that the positive correlation $\langle \tilde{\epsilon}_{jl}^{HI} \tilde{\epsilon}_{jl}^{DM} \rangle > 0$ becomes weaker on scales $j \geq 8$ or $k < 3$ h Mpc⁻¹ or $L > 2$ h⁻¹ Mpc. Since intermittent features become significant on scales $j \geq 8$, the dynamical assumption that $\rho_{HI}(\mathbf{x}) \propto \rho_{DM}^a(\mathbf{x})$ is applicable only for lower order statistics (like the power spectrum.)

6. Comparison of intermittent features between real and simulation samples

6.1. Structure functions of real and simulation samples

We now calculate the structure functions for the transmitted flux fluctuations of the simulation samples. The results are illustrated in Fig. 8 for HS1700 and Fig. 9 for q0014. The error bars are the 1- σ deviations estimated from the 1000 simulation samples. Comparing Figs. 8 and 9 with Fig. 2, we see that $\ln S_j^{2n}/(S_j^2)^4$ with $n = 2$ has smaller errors than the power spectrum. Even at 6th and 8th orders, the j -dependence of $\ln S_j^{2n}/(S_j^2)^n$ can be very well fitted by a line. This implies that to measure the higher order statistical behavior of an intermittent field, the structure functions are effective and stable. For an intermittent field, the large uncertainty in the power spectrum are caused by rare and improbable high spikes in the fluctuations. However, the structure function is an ensemble average of the ratio between S_j^{2n} and $(S_j^2)^n$ and this reduces the

effect of individual high spikes.

Figures 8 and 9 also show that for a given n , $\ln S_j^{2n}/(S_j^2)^n$ increases with scale j so that the intermittent exponent ζ [eq.(21)] is non-zero and negative. The transmitted flux fluctuations are, hence, intermittent. In Fig. 10, we show $\ln S_j^{2n}/(S_j^2)^n$ vs. j of HS1700 mock samples produced by both the 12 and 6 h^{-1} Mpc box. The 12 h^{-1} Mpc samples is a little higher $\ln S_j^{2n}/(S_j^2)^n$, but there are no significant differences between the simulation samples on scales considered.

The structure functions measured for the real data of HS1700 is also shown in Fig. 10, in which the error bars HS1700 are found by bootstrap re-sampling. Within the error bars, the observed structure function is consistent with the 12 Mpc box simulation samples for the LCDM model. Although the consistency shown in Fig. 10 is still not perfect, it is substantially better than the results obtained from the pseudo hydro simulations. Pando et al (2002) found that the structure functions of the pseudo hydro simulation samples were generally larger than those of the real data [see Fig. 7 of Pando et al. (2002)].

The structure functions for both HS1700 and q0014 have similar behavior although they lie at different redshifts. The result demonstrates that one cannot see a significant redshift evolution in the range of $2 < z < 3$ with the j -dependence of the structure functions.

6.2. n -dependence of the structure function

We now turn to the n -dependence of the structure functions. Figures 11 and 12 are, respectively, $\ln S_j^{2n}/(S_j^2)^n$ vs. n for the simulation samples and real data of HS1700 and q0014 on scales $j = 9$ and 10. The figures show again that the simulation result is consistent with observations on the scales considered.

For a Gaussian field, the n -dependence of structure function is $\ln S_j^{2n}/(S_j^2)^n = \ln(2n - 1)!!$ [eq.(5)], which is also plotted in Figs. 11 and 12. We note, from Figs. 11 and 12, that although $\ln S_j^{2n}/(S_j^2)^n$ is above that of a Gaussian field, $\ln S_j^{2n}/(S_j^2)^n$ seems to “parallel” the Gaussian curve. This means that although the field on scale $j = 9$ is non-Gaussian, the PDF of $\tilde{\epsilon}_{jl}^F$ doesn’t have a significantly long tail. On scale $j = 10$, the slope of $S_j^{2n}/(S_j^2)^n$ becomes larger than $(2n - 1)!!$, which indicates that the PDF of $\tilde{\epsilon}_{jl}^F$ tends to be long tailed.

The n -dependence of $\ln S_j^{2n}/(S_j^2)^n$ appear to be more sensitive to redshift evolution. Figure 11 shows that the relation of $S_j^{2n}/(S_j^2)^n$ for $j = 9$ is clearly above the Gaussian field, while for Fig. 12 it is only marginally different from a Gaussian field. Thus, the intermittent behavior on scale $j = 9$ probably developed at redshift $z \leq 3$.

Similar to the power spectrum (Fig. 1), the results of Figs. 8 - 12 result is f -independent on the entire scale range considered for $f = 1$ to 3 (Pando et al 2002). To see the effect of metal lines, we plot Fig. 13, which shows the n -dependence of $\ln S_j^{2n}/(S_j^2)^n$ ($j = 10$) with and without metal line removal. The result for $j = 10$ is less affected by the metal line removing because most metal

lines have width less than $\Delta v = 32$ km/s ($j = 10$).

6.3. Intermittent exponent

The n -dependence of the intermittent exponent ζ can be calculated by eq.(17), which gives

$$\zeta(n) = -\frac{1}{j} \ln_2 \frac{S_j^{2n}}{(S_j^2)^n} + \text{const}, \quad (26)$$

or

$$\zeta(n) - \zeta(1) = -\frac{1}{j} \ln_2 \frac{S_j^{2n}}{(S_j^2)^n}. \quad (27)$$

For the simulation samples, the relation of $\ln_2 S_j^{2n}/(S_j^2)^n$ vs. n shown in Fig. 10 can be very well fitted by a line in the range from $j = 7$ to 10 (or $2 \leq k \leq 16$ h Mpc⁻¹), and therefore, one can find a constant $\zeta(n)$ for each given n . The real data is not as well fitted over the same scales, but we nonetheless show the results in figures 14 and 15.

Again the full hydro simulation shows better result than the pseudo hydro simulation. The value of $|\zeta|$ for the real data is found to be systematically lower than that given by pseudo hydro simulation for the LCDM models (Pando et al. 2002). Although, the value $|\zeta|$ from the hydro simulation is still higher than real data, the differences are no longer larger than the error bars for all n . Figure 16 shows the intermittent exponent for samples with 12 and 6 h⁻¹Mpc boxes. Note that the conclusions drawn from Figs. 14 and 15 hold also for samples with the 6 h⁻¹Mpc box.

6.4. Intermittency of HI density field

It has been argued that the intermittency of the Ly α transmitted flux field $F(\lambda)$ may not indicate intermittency in the IGM distribution $\delta_b(\lambda)$ or HI distribution $\delta_{HI}(\lambda)$. The reason is that in the exponential relation between the flux and optical depth $F(\lambda) = F_c e^{-\tau(\lambda)}$, and the optical depth $\tau(\lambda)$ is approximately related to $\delta_b(\lambda)$ by

$$\tau(\lambda) = A[\rho_b(\lambda)/\bar{\rho}_b]^a = A[1 + \delta_b(\lambda)]^a, \quad (28)$$

where the parameter A depends on the cosmic baryonic density, the photoionization rate of HI, and the temperature of IGM. Therefore, even when $\delta_b(\lambda)$ or $\delta_{HI}(\lambda)$ are Gaussian, the PDF of the flux $F(\lambda)$ might be lognormal due to the exponential relation between $F(\lambda)$ and $\delta_{HI}(\lambda)$.

However as has been emphasized in §2, the intermittency of $F(\lambda)$ field is not measured by the PDF of $F(\lambda)$, but its difference $\Delta_{\delta\lambda} F(\lambda) \equiv F(\lambda + \delta\lambda) - F(\lambda)$. The structure functions are defined by the density difference. Thus, we have approximately

$$\Delta_{\delta\lambda} F(\lambda) \simeq -e^{-\tau(\lambda)} \Delta_{\delta\lambda} \tau(\lambda) \quad (29)$$

where $\Delta_{\delta\lambda}\tau(\lambda) \equiv \tau(\lambda + \delta\lambda) - \tau(\lambda)$. Using eq.(27), we have

$$\Delta_{\delta\lambda}\tau(\lambda) \simeq -Aa[1 + \delta_H(\lambda)]^{a-1}\Delta_{\delta\lambda}\delta_b(\lambda), \quad (30)$$

where $\Delta_{\delta\lambda}\delta_b(\lambda) \equiv \delta_b(\lambda + \delta\lambda) - \delta_b(\lambda)$.

Eqs.(29) and (30) show that if the transmitted flux fluctuations are intermittent, the baryonic matter density field and HI field should also be intermittent (Zhan, Jamkhedkar, & Fang 2001). Figure 17 presents the structure functions for the HI field of the 12 Mpc box samples simulation and shows that the HI field is indeed intermittent. In fact, this field has larger structure functions than the flux fluctuations probably because the transmitted flux cannot trace the intermittency of optical depth at heavy absorption regions.

7. Discussion and conclusions

We analyzed the intermittent behavior of the Ly α transmitted flux fluctuations of real data and samples produced by full hydro simulations. This analysis covers scales from $\sim 10 \text{ h}^{-1} \text{ Mpc}$ to $400 \text{ h}^{-1} \text{ kpc}$ ($j = 6$ to 10), and statistical orders $2n$ from 2 to 8. The intermittent behavior is found to be significant on scales less than about $\sim 1 \text{ h}^{-1} \text{ Mpc}$, and redshift $z \leq 3$. Over the entire scale range and statistical orders considered, the intermittent behavior of the real data matches the samples produced by full hydrodynamic simulations in the LCDM model.

We have shown that the point-by-point correlation of the IGM and HI fields with dark matter field becomes weaker on scales less than about $2 \text{ h}^{-1} \text{ Mpc}$, which is much larger than the Jeans length at the mean density. Although the power spectrum of the IGM field is still about the same as that of dark matter at these scales, the mass density field of the IGM is no longer point-by-point proportional to the underlying dark matter field.

By using intermittency we have detected a the dynamical discrepancy between the IGM field and the dark matter distribution. The study of cosmic large scale structure has mainly concentrated on either the two-point correlation function and its scaling, or on the massive collapsed halos of dark matter. Intermittency may bridge the gap between the two approaches and provide new, physically interesting insights in cosmic clustering.

We thank Dr. D. Tytler for kindly providing the data of the Keck spectrum HS1700+64 and q0014+8118, and Dr. W. Zheng for providing the metal-line identification of HS1700+64. Dr. Jamkhedkar is acknowledged for her help, especially, Figure 1 which is taken from her thesis. We thank also Dr. D. Weinberg for comments and suggestions in his referee's report. LLF acknowledges support from the National Science Foundation of China (NSFC) and National Key Basic Research Science Foundation.

A. Dynamical equations of the IGM and dark matter mass field

A.1. Basic equations

Let us consider a flat universe having cosmic factor $a(t) \propto t^{2/3}$ and dominated by dark matter. We describe the dark matter by a mass density field $\rho(\mathbf{x}, t)$ and a peculiar velocity field $\mathbf{v}(\mathbf{x}, t)$, where \mathbf{x} is the comoving coordinate. In hydrodynamical descriptions, the equations of dark matter consist of the continuity, the momentum, and the gravitational potential equations as follows (Wasserman 1978)

$$\frac{\partial \delta}{\partial t} + \frac{1}{a} \nabla \cdot (1 + \delta) \mathbf{v} = 0 \quad (\text{A1})$$

$$\frac{\partial a \mathbf{v}}{\partial t} + (\mathbf{v} \cdot \nabla) \mathbf{v} = -\nabla \phi \quad (\text{A2})$$

$$\nabla^2 \phi = 4\pi G a^2 \bar{\rho} \delta \quad (\text{A3})$$

where density perturbation $\delta(\mathbf{x}, t) = [\rho(\mathbf{x}, t) - \bar{\rho}]/\bar{\rho}$, and the mean density $\bar{\rho} = 1/6\pi G t^2 \propto a^{-3}$. The peculiar gravitational potential ϕ is zero (or constant) when density perturbation $\delta = 0$. The operator ∇ is acting on the comoving coordinate \mathbf{x} . For the growth mode of the perturbations, the velocity is irrotational. In this case, one can define a velocity potential by

$$\mathbf{v} = -\frac{1}{a} \nabla \varphi \quad (\text{A4})$$

With this potential, the momentum equation (A2) can be rewritten as the Bernoulli equation

$$\frac{\partial \varphi}{\partial t} - \frac{1}{2a^2} (\nabla \varphi)^2 = \phi. \quad (\text{A5})$$

Since there is only gravitational interaction between dark matter and the IGM or cosmic baryonic gas, it is convenient to describe the IGM by its mass density field $\rho_b(\mathbf{x}, t)$ and velocity field $\mathbf{v}_b(\mathbf{x}, t)$. The hydrodynamical equations of the IGM are

$$\frac{\partial \delta_b}{\partial t} + \frac{1}{a} \nabla \cdot (1 + \delta_b) \mathbf{v}_b = 0 \quad (\text{A6})$$

$$\frac{\partial a \mathbf{v}_b}{\partial t} + (\mathbf{v}_b \cdot \nabla) \mathbf{v}_b = -\frac{1}{\rho_b} \nabla p_b - \nabla \phi \quad (\text{A7})$$

where the density perturbation of the IGM $\delta_b(\mathbf{x}, t) = [\rho_b(\mathbf{x}, t) - \bar{\rho}_b]/\bar{\rho}_b$, and $\bar{\rho}_b$ the mean density of the IGM. The gravity of the IGM is negligible. The evolution of the IGM is governed by the gravitation of dark matter, and therefore, the gravitational potential ϕ in eq.(A7) is still given by eq. (A3).

To sketch the gravitational clustering of the IGM, we will not consider the details of heating and cooling. Thermal processes are generally local, and therefore, it is reasonable to describe the thermal processes by a polytropic relation $p_b(\mathbf{x}, t) \propto \rho_b^\gamma(\mathbf{x}, t)$. Thus eq.(A7) becomes

$$\frac{\partial a \mathbf{v}_b}{\partial t} + (\mathbf{v}_b \cdot \nabla) \mathbf{v}_b = -\frac{\gamma k_B T}{\mu m_p} \frac{\nabla \delta_b}{(1 + \delta_b)} - \nabla \phi \quad (\text{A8})$$

where the parameter μ is the mean molecular weight of IGM particles, and m_p the proton mass. In this case, we don't need the energy equation and the IGM temperature evolves as $T \propto \rho^{\gamma-1}$, or $T = T_0(1 + \delta_b)^{\gamma-1}$. Eq.(A8) is different from eq.(A2) only by the term with temperature T . If we treat this term in the linear approximation, we have

$$\frac{\partial \varphi_b}{\partial t} - \frac{1}{2a^2}(\nabla \varphi_b)^2 - \frac{\nu_b}{a^2} \nabla^2 \varphi_b = \phi, \quad (\text{A9})$$

where φ_b is the velocity potential for IGM field defined by

$$\mathbf{v}_b = -\frac{1}{a} \nabla \varphi_b. \quad (\text{A10})$$

The coefficient ν_b is given by

$$\nu_b = \frac{\gamma k_B T_0}{\mu m_p (d \ln D(t)/dt)}, \quad (\text{A11})$$

where $D(t)$ describes the linear growth behavior.

Eq.(A9) shows that the clustering of the IGM field is completely controlled by the gravity of underlying mass fields of dark matter. It can then be considered as a "passive substance" with respect to the underlying dark matter. The term with ν_b in eq.(A9) acts like a viscosity which is due to thermal diffusion characterized by the Jeans length $k_J^2 = (a^2/t^2)(\nu m_p/\gamma k_B T_0)$. In linear regime, eqs.(A5) and (A9) yield solution $\varphi_b = \varphi$ on scales larger than the Jeans length.

A.2. Equation of the difference between the IGM and dark matter fields

To study the possible difference between the IGM and dark matter, we define a variable Θ by

$$\Theta = \varphi_b - \varphi \quad (\text{A12})$$

which describes the deviation of IGM from dark matter. With eqs. (A5) and (A9), we have

$$\frac{\partial \Theta}{\partial t} - \frac{1}{2a^2}(\nabla \Theta)^2 - \frac{\nu_b}{a^2} \nabla^2 \Theta = \frac{\nu_b}{a^2} \nabla^2 \varphi + \frac{1}{a^2}(\nabla \Theta)(\nabla \varphi). \quad (\text{A13})$$

When $\nu_b = 0$, this has solution $\Theta = \text{const}$, if the initial condition is $\Theta = \text{const}$. During linear evolution, we have $\Theta = 0$, and therefore $\Theta = 0$ is the initial condition for eq.(A13). Thus, the solution $\Theta = 0$ is correct even in the nonlinear regime if $\nu_b = 0$. There is no deviation of IGM from dark matter.

In the case of $\nu_b \neq 0$, $\Theta = 0$ will no longer be the solution of eq.(A13) even if it is $\Theta = 0$ initially. Considering that the potential φ of dark matter essentially is stochastic, the r.h.s. of eq.(13) plays the role of stochastic forces. It drives Θ to be non-zero. This leads to a statistical or stochastic discrepancy of the IGM field from dark matter field. This discrepancy is not trivial even when we consider the linear approximation of eq.(A13) with respect to Θ , i.e.

$$\frac{\partial \Theta}{\partial t} - \frac{1}{a^2}(\nabla \Theta)(\nabla \varphi) - \frac{\nu_b}{a^2} \nabla^2 \Theta = \frac{\nu_b}{a^2} \nabla^2 \varphi. \quad (\text{A14})$$

Eq.(14) essentially is the same as that widely used to dynamically model the discrepancy, or decoupling, of the statistical properties of the passive substance from the underlying field (for a review, Shraiman & Siggia, 2001). Since the advection term $\frac{1}{a^2}(\nabla\Theta)(\nabla\varphi)$ doesn't depend on the diffusion scales, the statistical discrepancy of the passive substance from the underlying field can appear on scales larger than the diffusion scale.

The field Θ given by eqs.(A13) and (A14) is generally intermittent. It has been shown that the field Θ given by eq.(A14) will be intermittent, even when the field φ is Gaussian (Kraichnan, 1994). Eq.(A13) is similar to the stochastic-force-driven Burgers' equation, or the so-called KPZ equation (Kardar, Parisi, & Zhang 1986, Berera & Fang 1994, Barabási, & Stanley, 1995, Jones 1999), which is typical of the dynamical model of intermittency (Polyakov 1995; Balkovsky et al. 1997; E et al. 1997). Therefore, the difference between the IGM and dark matter fields, Θ , is probably intermittent.

REFERENCES

- Balkovsky, E., Falkovich, G., Kolokolov, I. & Lebedev, V. 1997, *Phys. Rev. Lett.* 78, 1452
- Barabási, A.L. & Stanley, H.E. 1995, *Fractal Concepts in Surface Growth*, (Cambridge Univ. Press)
- Batchelor, G.K. & Townsend, A.A., 1949, *Proc. R. Soc. Lond. A* 199, 238
- Berera, A. & Fang, L.Z. 1994, *Phys. Rev. Lett.*, 72, 458
- Bi, H.G. 1993, *ApJ*, 405, 479
- Bi, H.G., Börner, G. & Chu, Y. 1992, *A&A*, 266, 1
- Bi, H.G. & Davidsen, A. F. 1997, *ApJ*, 479, 523.
- Bi, H.G., Ge, J. & Fang, L.Z. 1995, *ApJ*, 452, 90
- Cen, R.Y., 1992, *ApJS*, 78, 341
- Daubechies I. 1992, *Ten Lectures on Wavelets* (Philadelphia: SIAM)
- Donoho, D.L. 1995, *IEEE Transactions on Information Theory*, 41, 613
- Eisenstein, D.J. & Hu, W., 1999, *ApJ*, 511, 5
- E., W., Khanin, K., Mazel, A. & Sinai, Y. 1997, *Phys. Rev. Lett.* 78, 1904
- Fang, L.Z. & Feng, L.L. 2000, *ApJ*, 539, 5
- Fang, L.Z. & Thews, R. 1998, *Wavelet in Physics* (Singapore: World Scientific)
- Fang, Y.H., Duncan, R.C., Crofts, A.P.S. & Bechtold, J. 1996, *ApJ*, 462, 77
- Feng, L.L. Pando, J. & Fang, L.Z. 2001, *ApJ*, 555, 74

- Feng, L.L., Shu C.W. & Zhang M.P., 2002, in Proceeding of 5th Sino-Germany Workshop on Cosmology and Galaxy Formation: The Formation, Evolution and Distribution of Galaxies. Y.P. Jing & G. Borner (eds); astro-ph/0212577.
- Frish, U., 1995, *Turbulence*, (Cambridge Univ. Press)
- Gärtner, J. & Molchanov, S.A., 1990, Commun. Math Phys. 132, 613
- Hui, L., & Gnedlin, N.Y., 1997, MNRAS, 292, 27
- Jamkhedkar, P., 2002, Thesis, University of Arizona, <http://www.ece.umd.edu/priya>
- Jamkhedkar, P., Zhan, H. & Fang, L.Z. 2000, ApJ, 543, L1
- Jamkhedkar, P., Bi, H.G. & Fang, L.Z. 2001, ApJ, 561, 94
- Jiang, G. & Shu, C.W., 1996, J. Comput. Phys. 126, 202
- Jones, B.T., 1999, MNRAS, 307, 376
- Kardar, M, Parisi, G & Zhang, Y.C. 1986, Phys. Rev. Lett. 56, 342.
- Kirkman, D. & Tytler, D. 1997, ApJ, 484, 672
- Kraichnan, R.H., 1994, Phys. Rev. Lett. 72, 1016
- Matarrese, S. & Mohayaee, R. 2002, MNRAS, 329, 37
- Nusser, A., 2000, MNRAS, 317, 902.
- Pando, J & Fang, L.Z. 1996, ApJ, 459, 1
- Pando, J. & Fang, L.Z. 1998a, A&A, 340, 335
- Pando, J. & Fang, L.Z., 1998b, Phys. Rev. E57, 3593
- Pando, J., Feng, L.L., Jamkhedkar, P., Zheng, W., Kirkman, D., Tytler, D. & Fang, L.Z. 2002, ApJ, 574, 575
- Peebles, P. J. E., 1980, *The large scale structure of the universe*, (Princeton University Press)
- Polyakov, A.M. 1995, Phys. Rev. E52 6183
- Shraiman B.I. & Siggia, E.D. 2000, Nature, 405, 8
- Shu, C.W., 1998, Lecture Notes in Mathematics, in Advanced Numerical Approximation of Nonlinear Hyperbolic Equations, ed. Quarteroni, A. (Springer) 325,
- Vanmarcke, E.H. 1983, *Random Fields, analysis and synthesis*, (MIT Press, 1983).
- Walker, T.P., Steigman, G., Schramm, D.N., Olive, K.A. & Kang, H.S., 1991, ApJ, 376, 51,
- Zel'dovich, Ya.B., Ruzmaikin, A.A. & Sokoloff, D.D. 1990, *The Almighty Chance*, (World Scientific, Singapore)
- Zhan, H., Jamkhedkar, P. & Fang, L.Z. 2001, ApJ, 555, 58

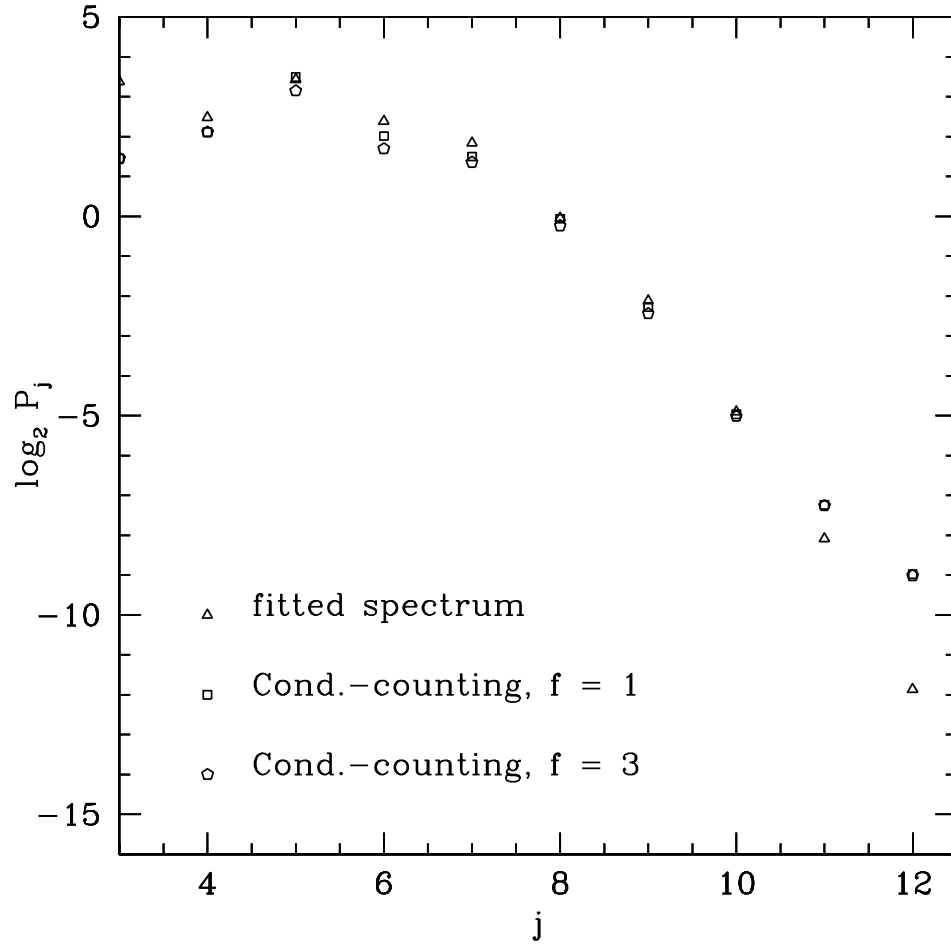


Fig. 1.— The power spectra of the HS1700+6416 transmitted flux for 1.) the fitted flux (triangle), 2.) conditional counting with $f = 1$ (square), and 3.) with $f = 3$ (pentagon). The physical scale for j is $\Delta v = 2^{13-j} \times 4$ km/s.

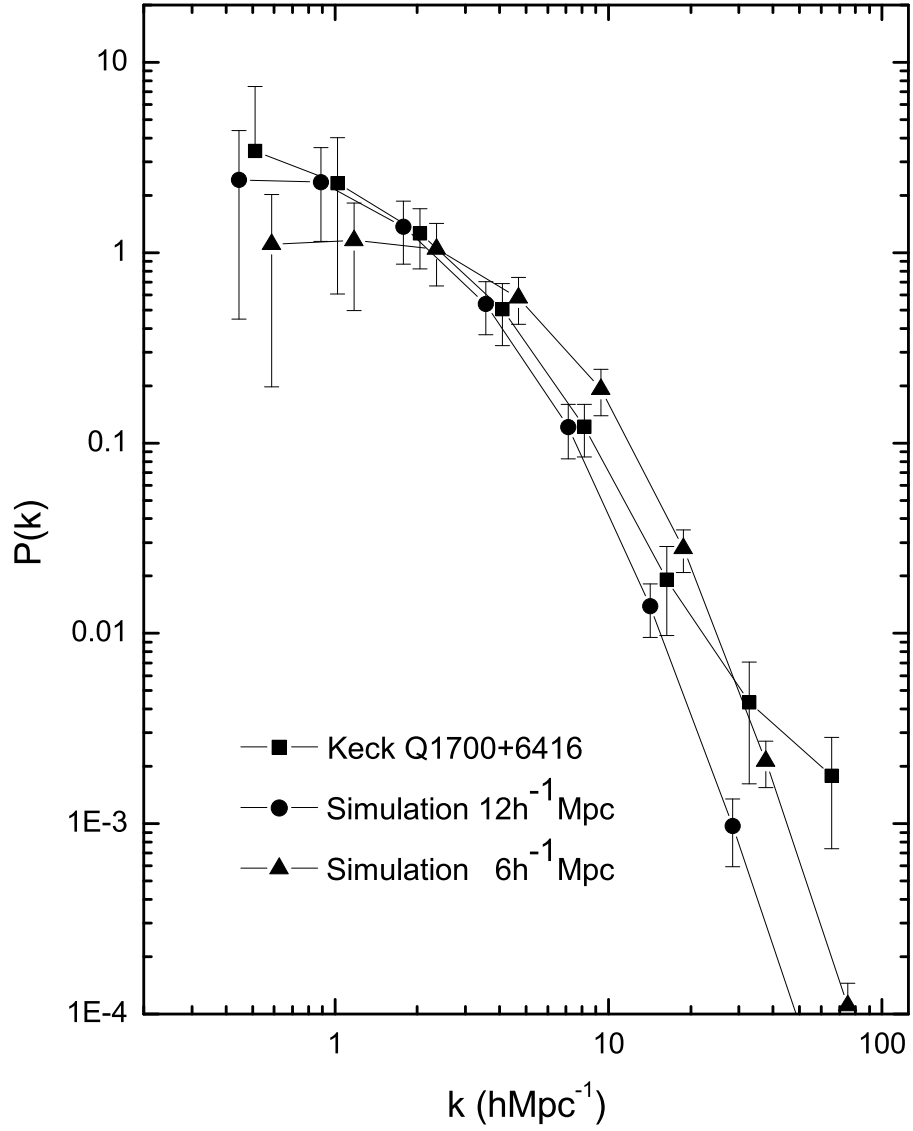


Fig. 2.— The power spectra of HS1700+6416 for 1.) real data (square); 2.) hydro simulation in a 12 Mpc box (circle), and 3.) in 6 Mpc box (triangle). The comoving wavenumber k is calculated in the LCDM model. For clarity, the power spectra of the simulations are shifted slightly.

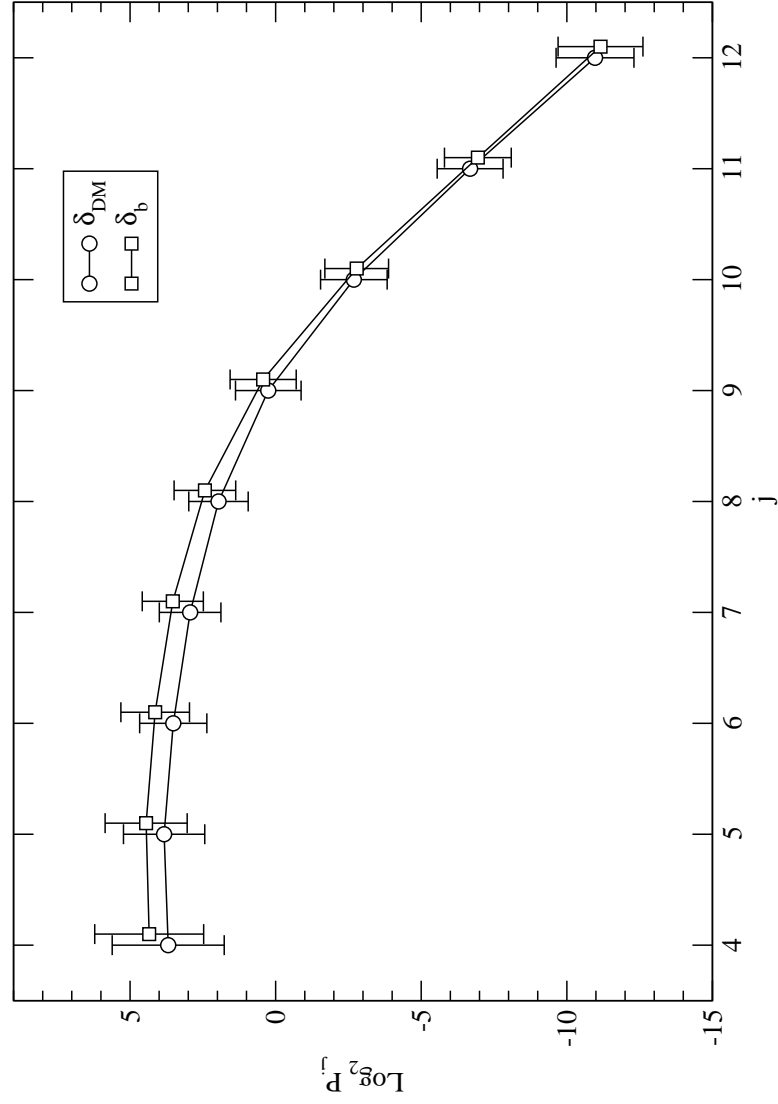


Fig. 3.— Power spectra of IGM mass field δ_b (square) and dark matter δ_{DM} (circle) from the hydro simulation in the 12 Mpc box. The mean and variance are calculated from the 100 realizations. The physical scale for j is $\Delta v = 2^{13-j} \times 4$ km/s. For clarity, the power spectrum of the IGM is shifted slightly.

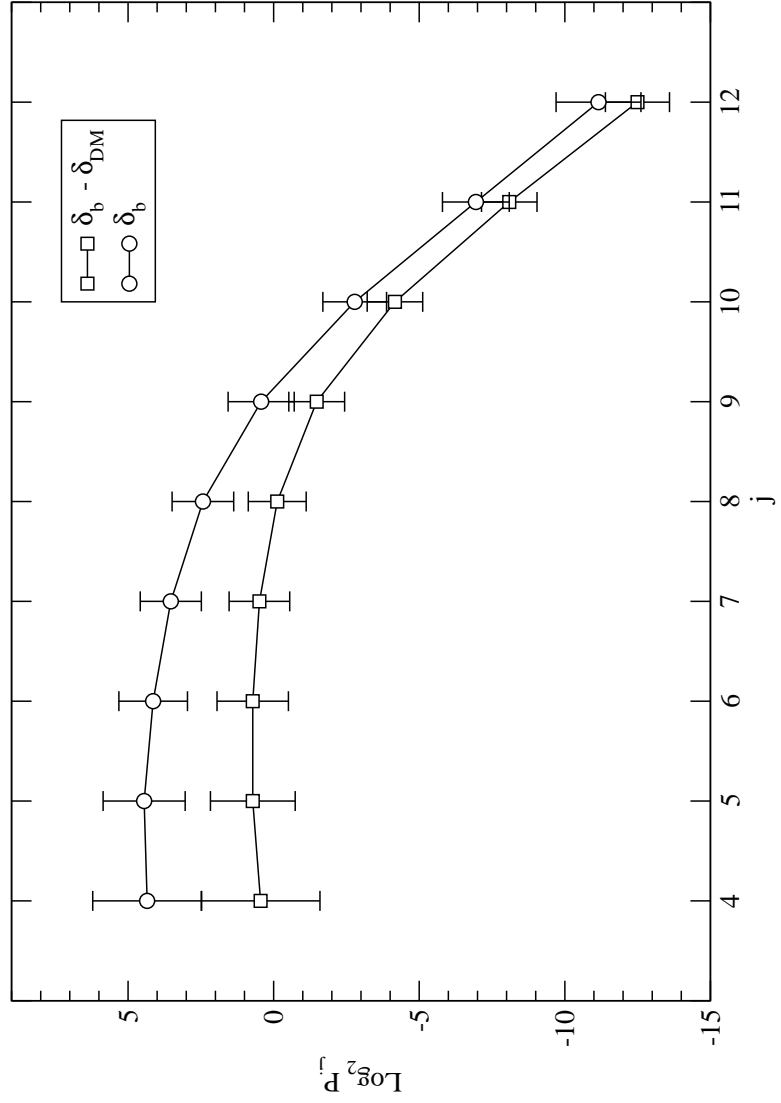


Fig. 4.— Power spectra of δ_b (circle) and $\delta_b - \delta_{DM}$ (square) of the hydro simulation samples for 12 Mpc box. The physical scales for j is $\Delta v = 2^{13-j} \times 4$ km/s.

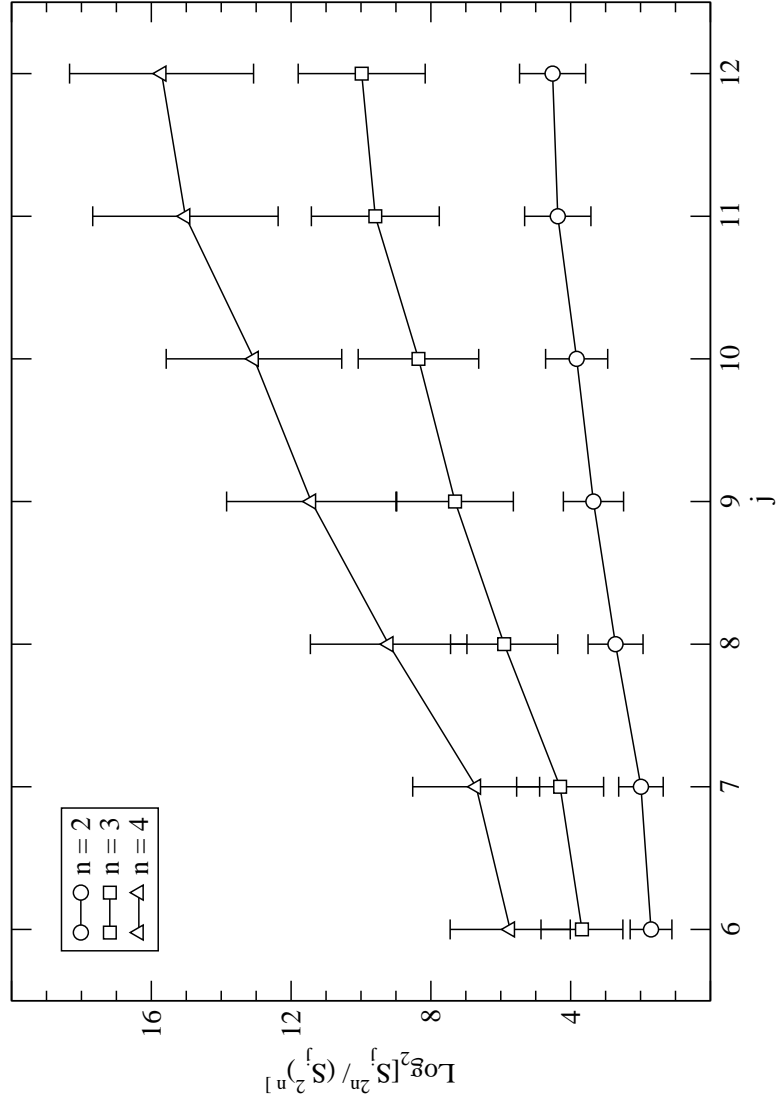


Fig. 5.— Structure functions $\ln_2[S_j^{2n}/(S_j^2)^n]$ vs. j of the difference $\delta_b - \delta_{DM}$ of the hydro simulation samples in the 12 Mpc box. The physical scale for j is $\Delta v = 2^{13-j} \times 4$ km/s.

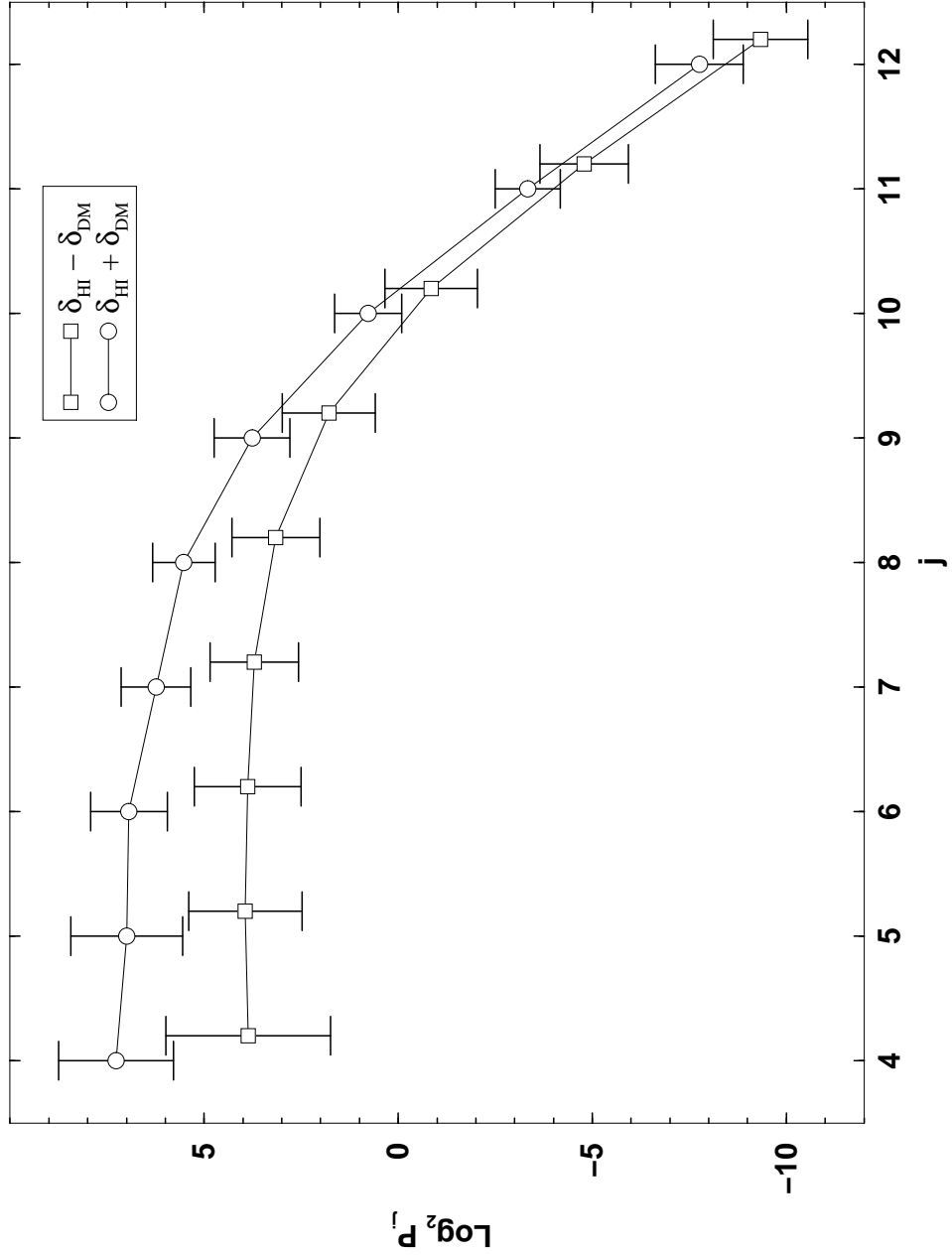


Fig. 6.— Power spectra of $\delta_{HI} + \delta_{DM}$ (circle) and $\delta_{HI} - \delta_{DM}$ (square) of the 12 Mpc box hydro simulation samples. The physical scale for j is $\Delta v = 2^{13-j} \times 4$ km/s. For clarity, the power spectrum of $\delta_{HI} - \delta_{DM}$ is shifted slightly.

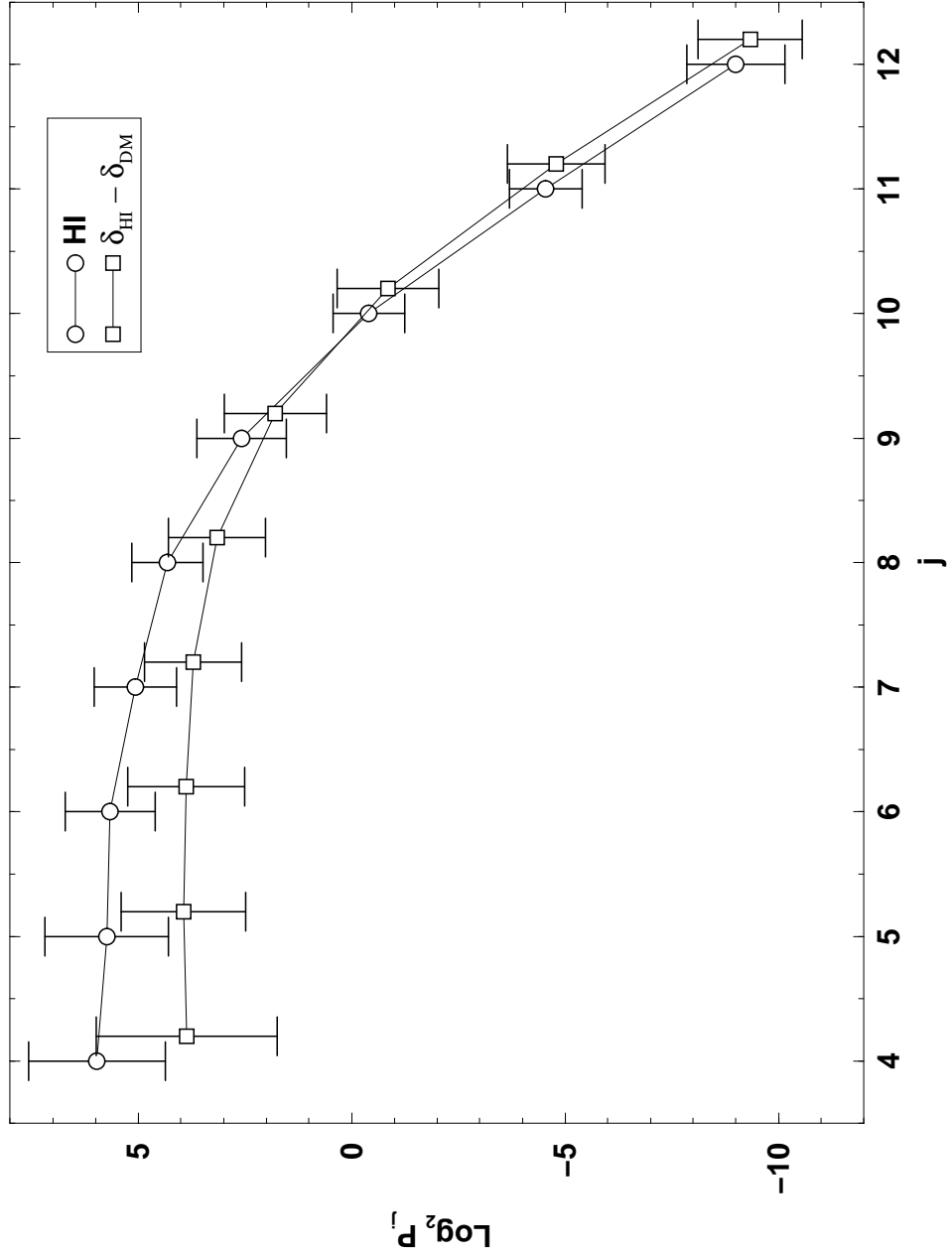


Fig. 7.— Power spectra of δ_{HI} (circle) and $\delta_{HI} - \delta_{DM}$ (square) of the 12 Mpc box hydro simulation samples. The physical scales for j is $\Delta v = 2^{13-j} \times 4$ km/s. For clarity, the power spectrum of $\delta_{HI} - \delta_{DM}$ is shifted slightly.

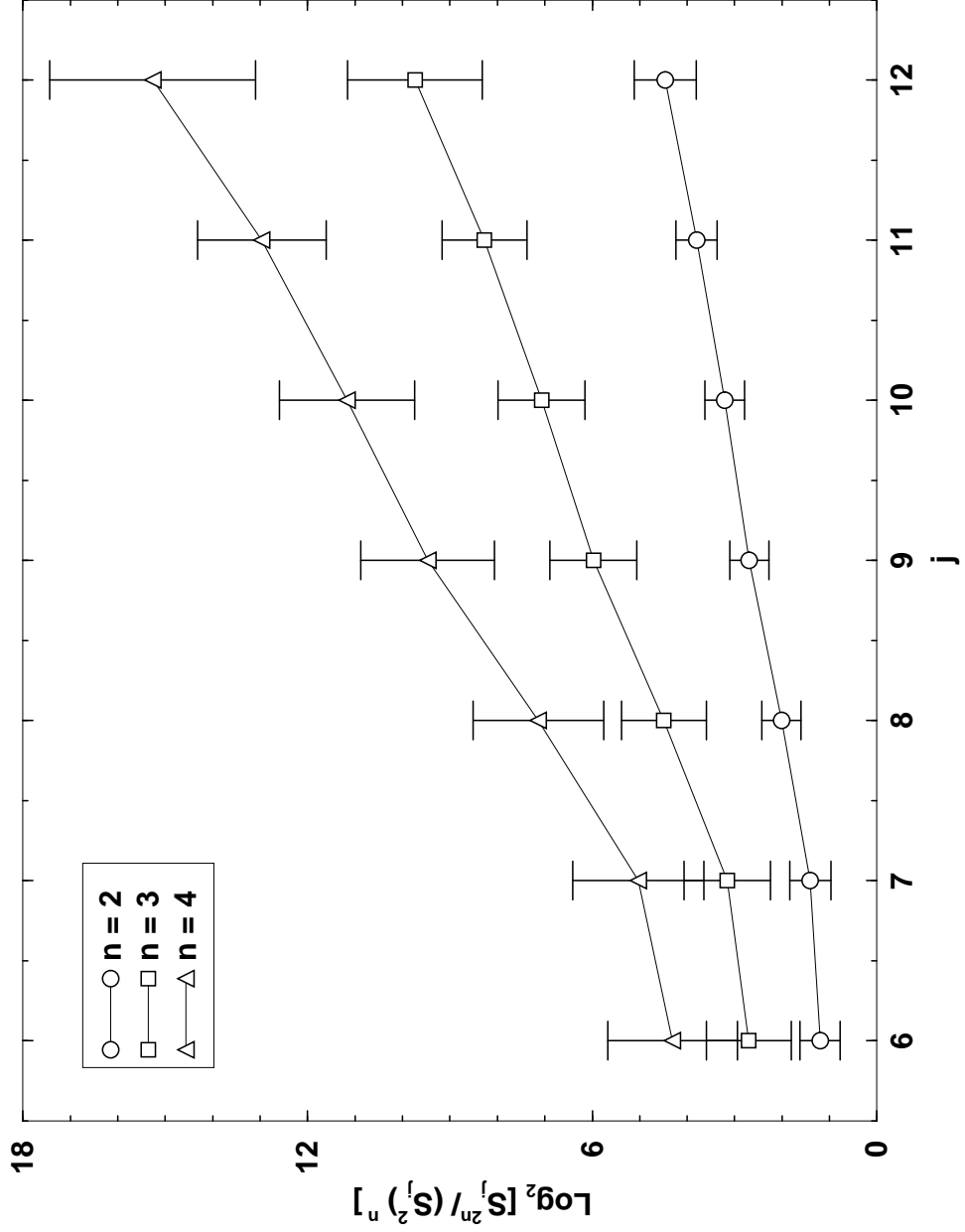


Fig. 8.— Structure functions $\ln_2[S_j^{2n}/(S_j^2)^n]$ vs. j of the hydro simulation samples for HS1700+6416 in the 12 Mpc box. The physical scale for j is $\Delta v = 2^{13-j} \times 4$ km/s.

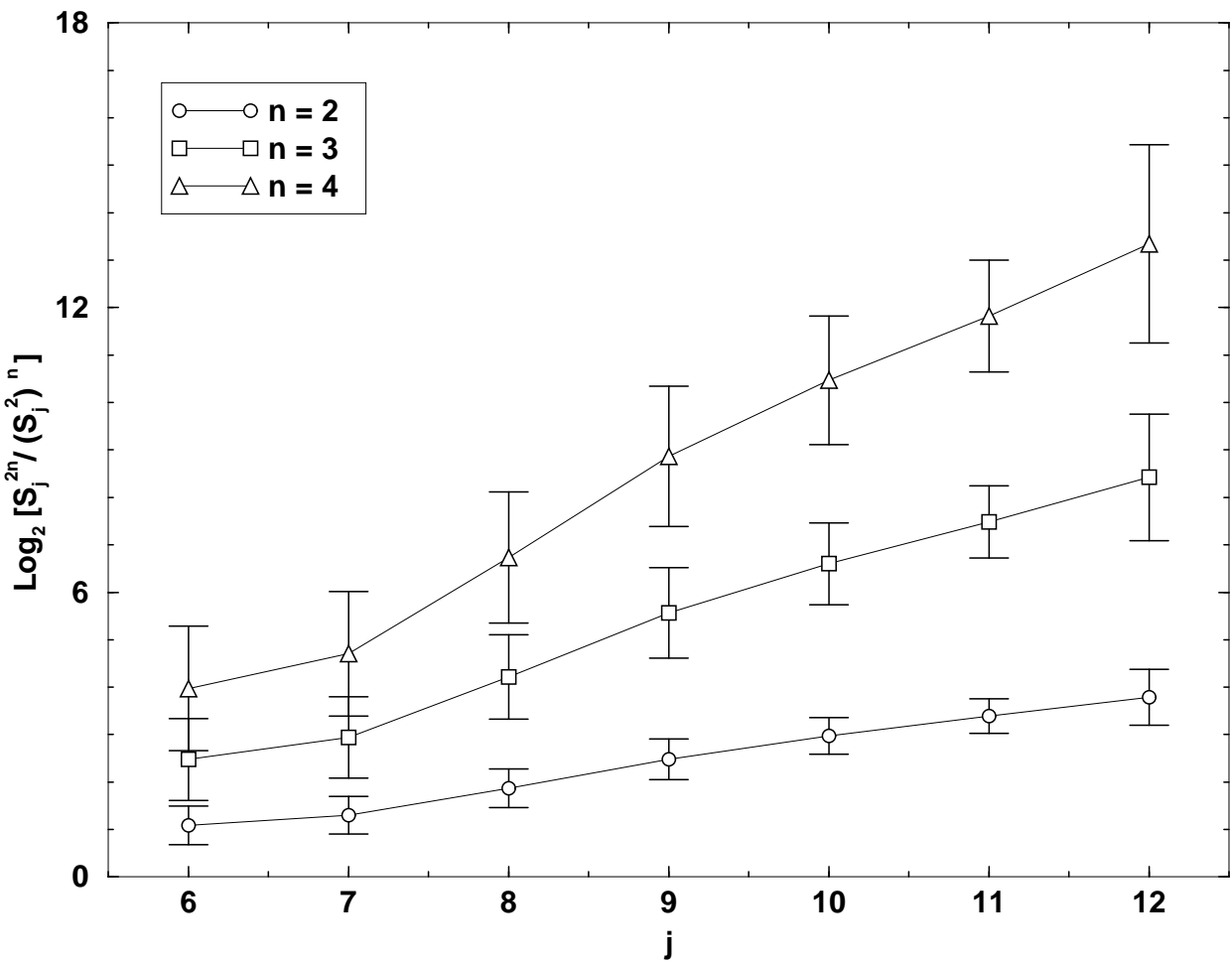


Fig. 9.— The same as Fig. 6, but for q0014+8118.

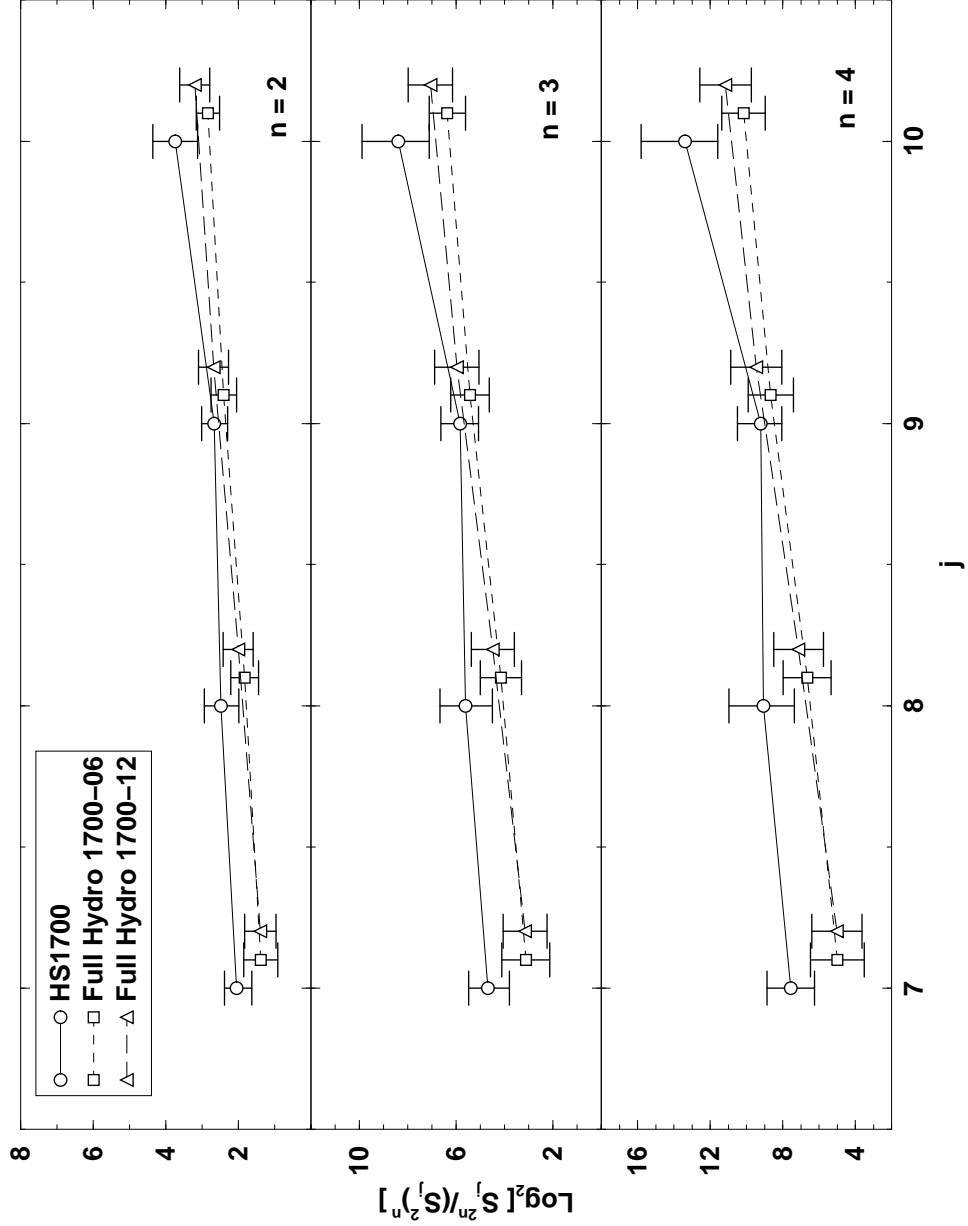


Fig. 10.— Structure function $\ln_2[S_j^{2n}/(S_j^2)]$ vs. j for HS1700+6416 of real data (circle) and hydro simulation with 12 (triangle) and 6 (square) Mpc box. The physical scale for j is $\Delta v = 2^{13-j} \times 4$ km/s. For clarity, the results of the two simulation samples are shifted slightly.

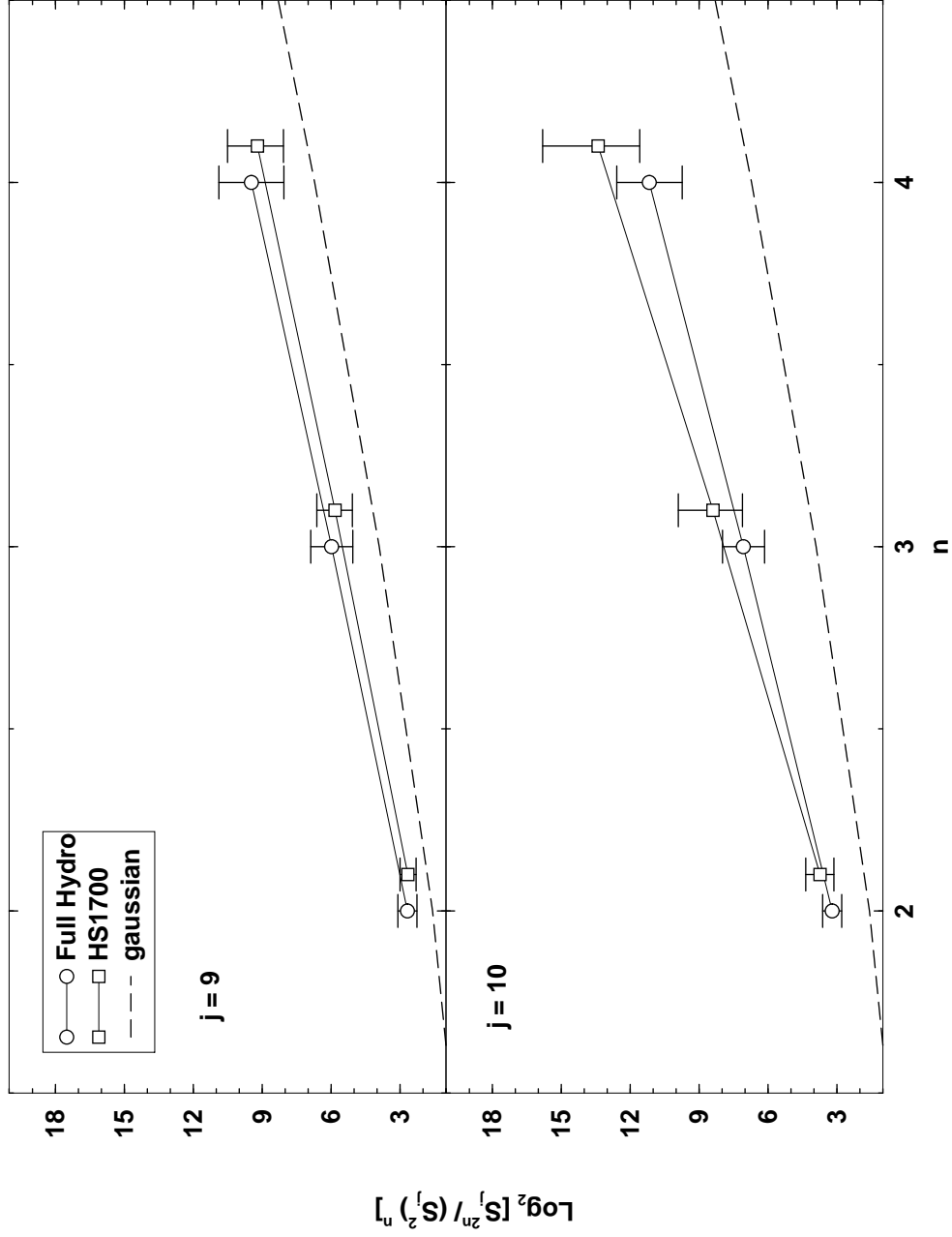


Fig. 11.— $\ln S_j^{2n}/(S_j^2)^n$ vs. n for simulation sample (circle) and real data (square) of HS1700+6416, and $j = 9$ and 10 , or $\Delta v = 64$ and 32 km/s. The dash line is for a Gaussian field. For clarify, the results of HS1700 data are shifted a little slightly.

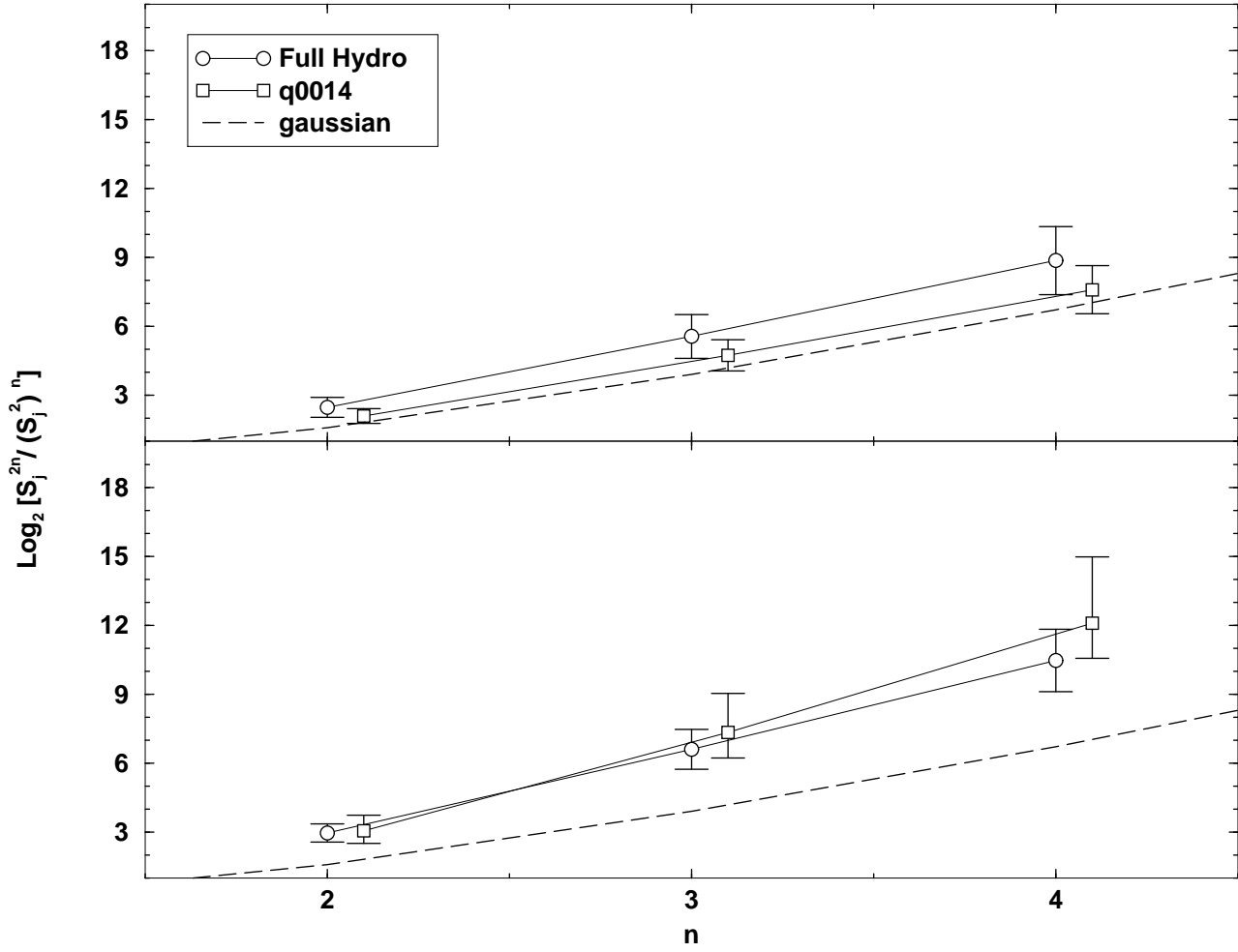


Fig. 12.— The same as Fig. 11, but for q0014+8118.

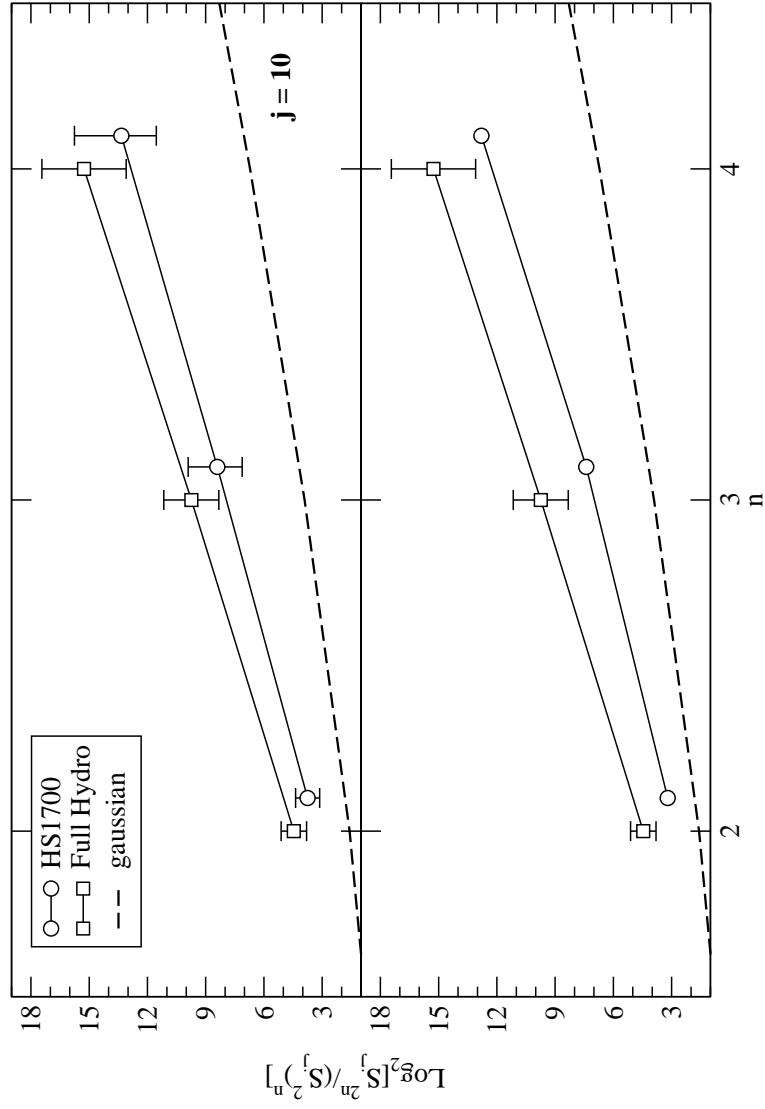


Fig. 13.— The same as Fig. 11 for $j = 10$. The top panel is for real data with metal line removing. The bottom panel is without metal line removing, which has about the same error bars as the top panel. The dash line is for a Gaussian field. For clarify, the results of HS1700 data are shifted a little slightly.

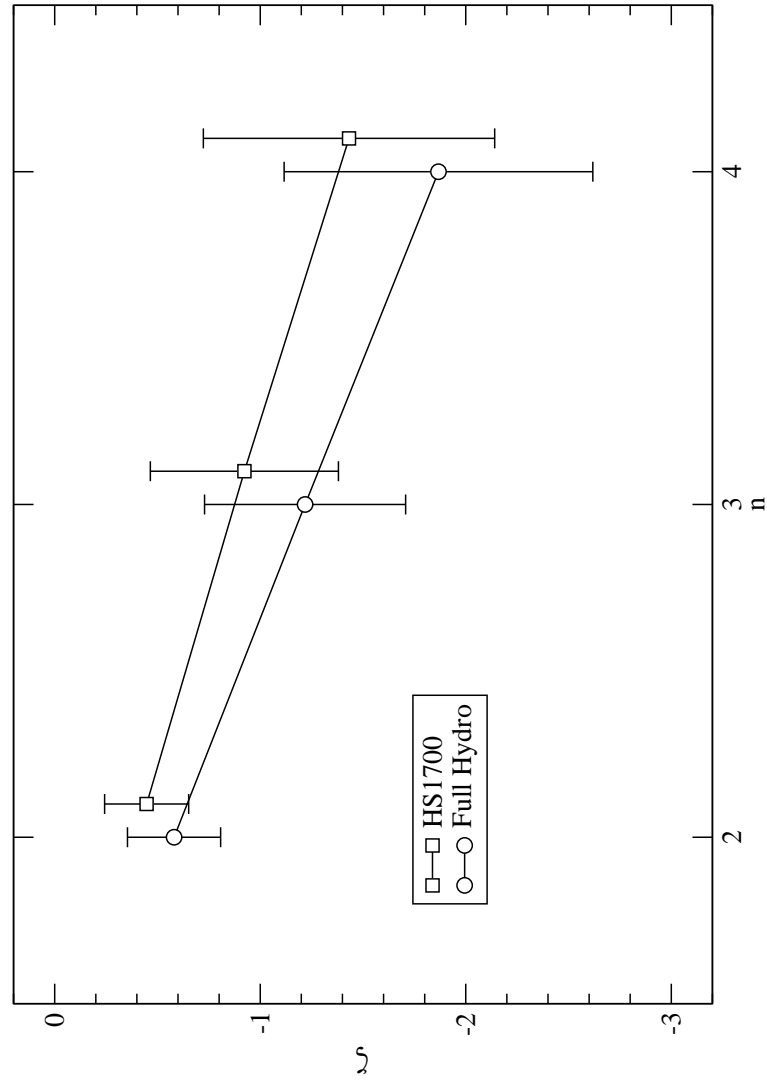


Fig. 14.— Intermittent exponent ζ vs. n for simulation data (circle) and real sample (square) of HS1700. For clarity, the results of HS1700 data are shifted a little bit to right.

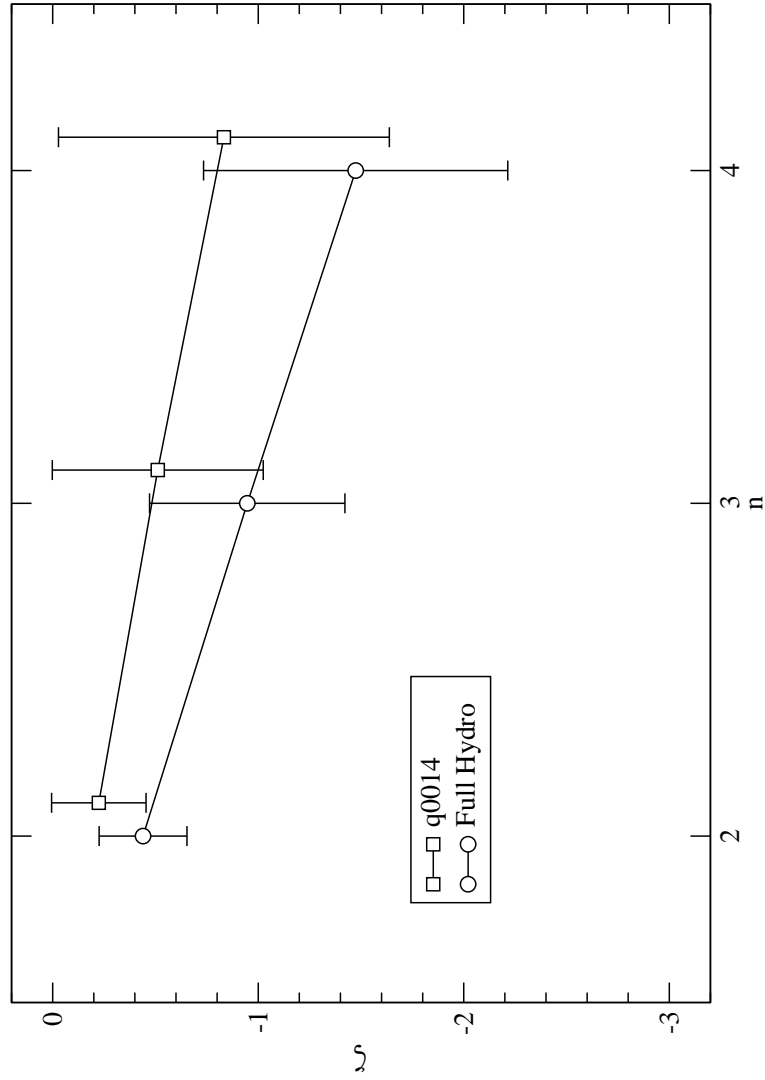


Fig. 15.— The same as Fig. 11, but for q0014+8118

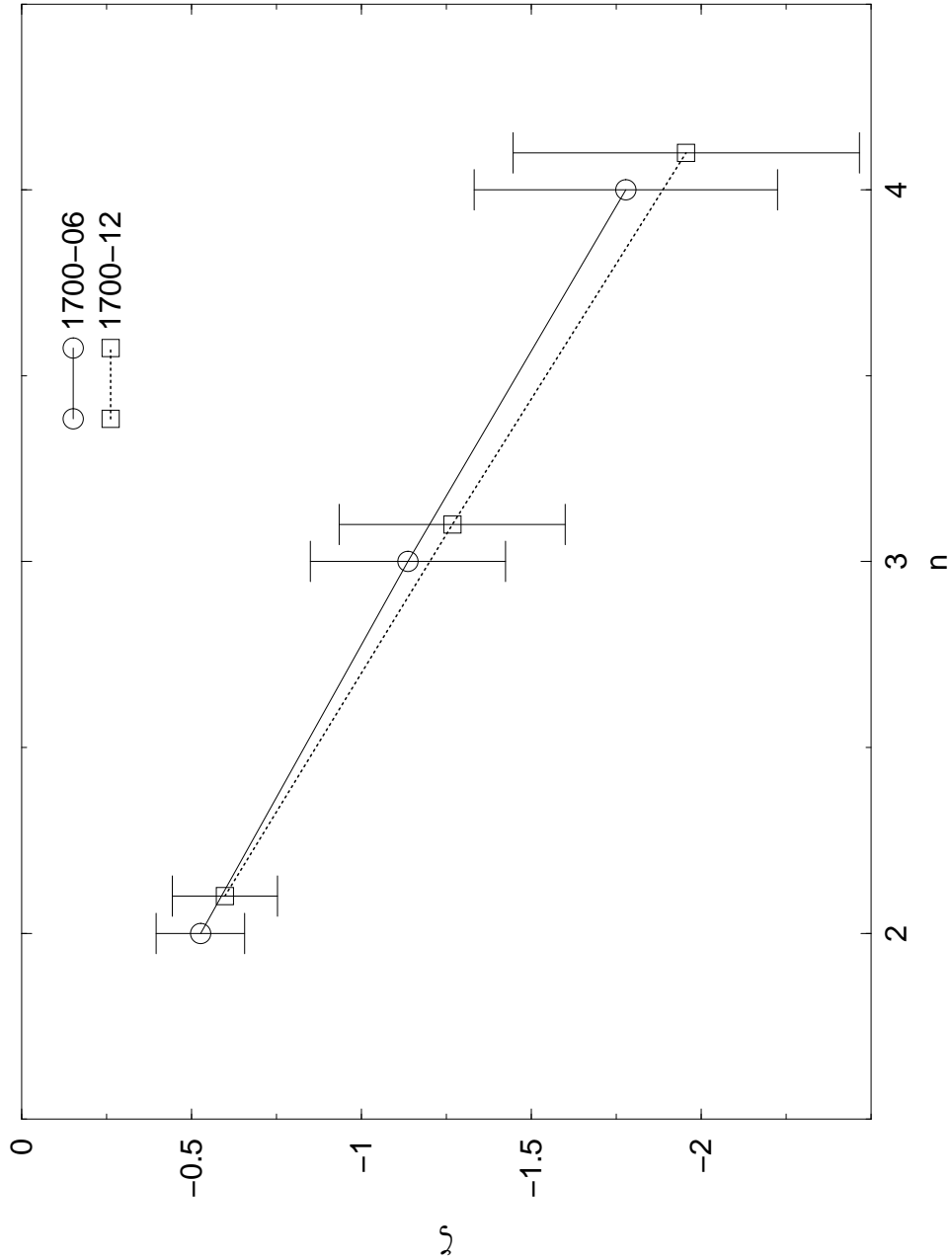


Fig. 16.— Intermittent exponent ζ vs. n of HS1700 samples given by hydro simulation in 12 (square) and 6 (circle) Mpc box. For clarify, the results for 12 Mpc box are shifted a little to the right.

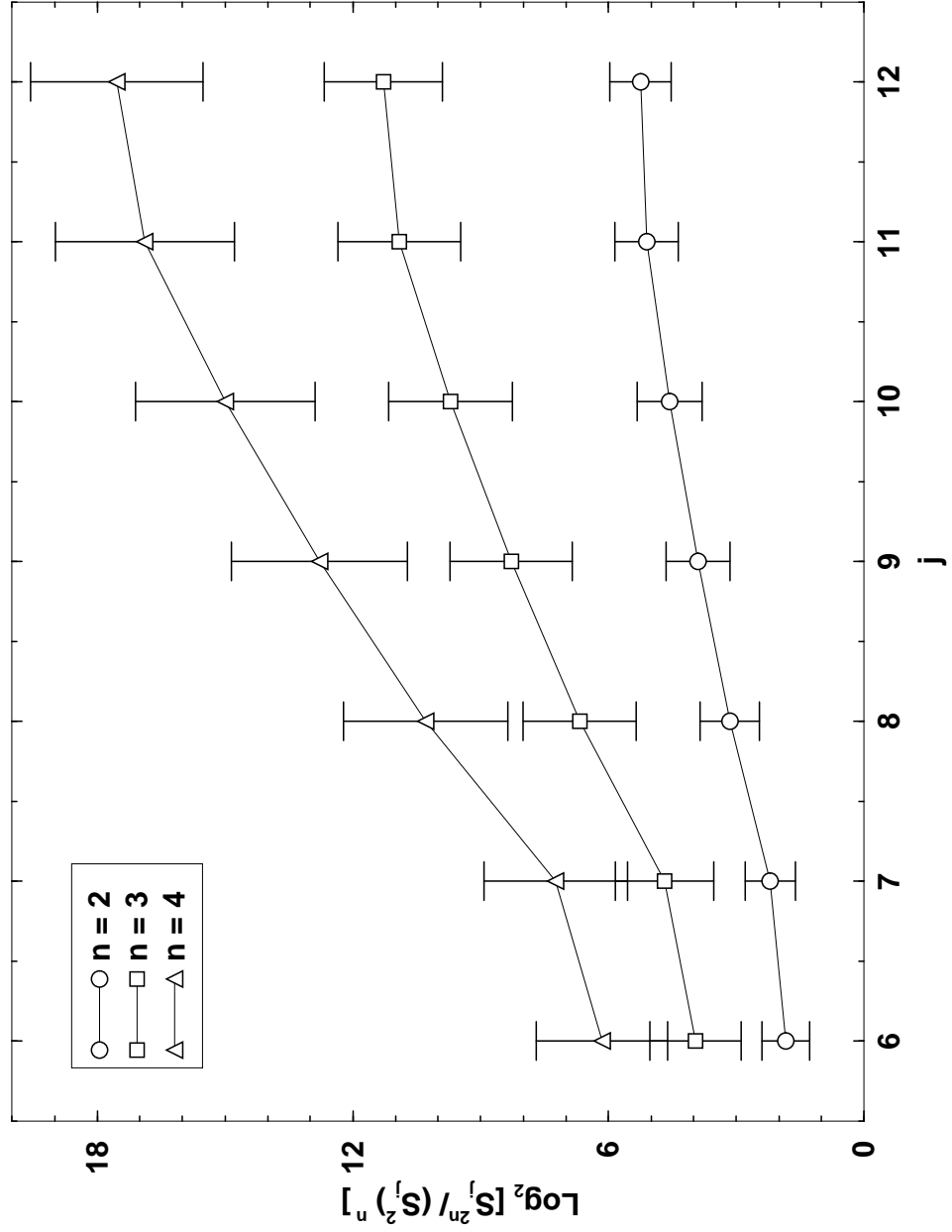


Fig. 17.— Structure functions $\ln_2[S_j^{2n}/(S_j^2)]$ vs. j of HI density field δ_{HI} . The physical scale for j is $\Delta v = 2^{13-j} \times 4$ km/s.